Title
The divergent outputs of Ire1 during the Unfolded Protein Response in fission yeast and budding yeast

Author
Crotty, Kelly

Publication Date
2019

The divergent outputs of Ire1 during the Unfolded Protein Response in fission yeast and budding yeast

by
Kelly J. Crotty

DISSERTATION
Submitted in partial satisfaction of the requirements for degree of
DOCTOR OF PHILOSOPHY

in

Biochemistry and Molecular Biology

in the

GRADUATE DIVISION
of the
UNIVERSITY OF CALIFORNIA, SAN FRANCISCO

Approved:

DocuSigned by:
Peter Walter
9C44B4D1D50740D...

Peter Walter
Chair

DocuSigned by:
Jeffery S. Cox
DocuSigned by:
John Gross
DocuSigned by:
Carol Gross
DocuSigned by:
Geeta Narlikar
EE2E6D32EE3043B...

Jeffery S. Cox
John Gross
Carol Gross
Geeta Narlikar
Committee Members

Acknowledgements.

I need to begin by acknowledging my mentor and adviser, Peter Walter. Peter's enthusiasm for discovery is boundless. He constantly challenged me to think more deeply and accept nothing at face value. I will always be grateful that he allowed me to rotate and accepted me into his lab, where I found endless opportunities. It was a privilege to work in Peter's Lab among the incredible group of scientists he curated.

Next, I need to acknowledge Weihan Li. He was my compatriot on Team *S. pombe* and a wonderful resource when I started my project in the Walter Lab. When it was clear that my original project would not yield a publishable story, he was incredibly generous to collaborate with me on his project. The new project required a set of skills I had never learned that he introduced me to in the short months leading up to his post-doc. Even after moving across the country, he made time to trouble-shoot with me remotely and continue our collaboration.

Mable Lam was my bay-mate, classmate, and roommate. I need to thank her for listening so patiently to me when experiments went wrong (which was frequently). She offered incredibly thoughtful advice when I needed to problem-solve and relatable humor when I just needed to vent. Along with her is Vlad Belyy, whose constant optimism and good mood elevated our bay and created an atmosphere that facilitated perseverance and passion. Thank you, Dynamic Bay!

Working in lab is hard and the graduate student brunch group (Aylin, Sandra, Mable, Han, and Karina) was essential to staying sane. Aylin, I need to give you a huge shout-out for giving me the push I needed to apply for the position I currently have. I never thought I would be accepted and I so, so appreciate you believing in me. Thank you, ladies, for your friendship and support!

I need to thank the members of the Book Club (Justin, Mable, Sandra, Chuck, Fernando, Candace, and Joselyn), as well, for accepting me into the group. Thank you to Chuck, especially, for inviting me into the club. At its height, our meetings were only ever half about the book and the other half was devoted to gossip and venting. It was validating to be in a group of such talented people and find out that we're all facing the same problems. Everyone is heading in different directions after grad school, and you all have my admiration.

I want to thank the Das Lab at Stanford for teaching me RNA biochemistry and giving me space in their lab for a few weeks as I did experiments. Clarence Cheng and Ann Kladwang were especially generous with their time and expertise.

It was intimidating to try Analytical Ultracentrifugation, so I need to thank Dyche Mullins for persuading me to go for it and for spending his valuable time analyzing the data with me. Dyche, you were a pleasure to work with.

As my project evolved, I added more and more people to my thesis committee until I had five members. In addition to Peter, I had Jeff Cox, John Gross, Carol Gross, and Geeta Narlikar. It was an honor just to have such talented investigators on my committee, but this group went above and beyond. It is no small feat to schedule five busy professors at once, but they made the time to have meetings as often as I needed one. They taught me a lot about thinking about the big picture and putting together a story. I am so grateful for their commitment to my success.

Other people who have played a role in supporting me on my way to graduation include Marc Shuman, who offered his time and advice while I was struggling both in lab and with my dad's cancer diagnosis. Christine Genero, Silke Nocke, Fran Sanchez, and Marivic Dinglasan are essential members of the lab who made sure everything happened behind the scenes. Fran and

Marivic were great sports when I needed to do 24-liter protein expressions with special media. Christine was always approachable and kind when I needed help and advice.

This brings me to my fiancé, Johnny Rodriguez. I need to thank and acknowledge Johnny for more things than I can fit here. So let me just say, Johnny, that you are the most talented scientist I know and you have taught me so much. I don't know if I would have made it through grad school without your support. Thank you for believing in me and making me always read the manual.

Lastly, my family. I am so lucky to have parents that believe in me with as much conviction as mine do. Thank you, mom, for always being on my side and never doubting for a moment that I would be successful. Your patience and conscientiousness inspire me. My dad never stopped giving advice and offering guidance. Even though he wasn't a biologist, he would find articles in my field to send to me. My whole life was a lesson from him on how to be a storyteller. Even though he didn't get to see me graduate, I know he was proud of me.

The divergent outputs of Ire1 during the Unfolded Protein Response in fission yeast and budding yeast

Kelly J. Crotty

Abstract.

In metazoans, the Unfolded Protein Response (UPR) restores homeostasis in the endoplasmic reticulum (ER) by both increasing the protein-folding capacity of the ER and by reducing the protein folding burden. The UPR in *S. cerevisiae* exclusively relies on this first solution to survive ER stress. Remarkably, *S. pombe* utilizes the second, though the UPR in both species is mediated through site-specific RNA cleavage by the evolutionarily conserved kinase/RNase transmembrane protein Ire1. While most of the *S. pombe* Ire1 mRNA substrates are degraded post cleavage, the mRNA encoding the ER chaperone protein BiP1 evades decay and the 5' fragment accumulates after truncation. Though the mechanism behind this stabilization remains unresolved, we have discovered that the relevance of *BIP1* mRNA processing to the cell's survival may be greater than previously estimated. We have compared the Ire1 kinase/RNase domain from each species *in vitro* and discovered key structural differences we can modulate to make the *S. cerevisiae* Ire1 behave like *S. pombe* Ire1. First, we characterized differences in cofactor sensitivity in the kinase domains of the two enzymes. Additionally, we exploited the toxicity of *S. pombe* Ire1 in bacterial cells to identify mutations in the more stringent *S. cerevisiae* Ire1 protein that would cause toxicity and relax substrate stringency. We identified a pair of mutations at the RNase dimer interface that expanded the *S. cerevisiae* enzyme's substrate repertoire and coincided with an increase in its propensity to dimerize. This interface could represent an under-utilized target for drug design to modulate the RNase activity of metazoan Ire1.

Table of Contents.

List of Figures

List of Tables.

Chapter One

Stabilization of truncated *BIP1* mRNA during ER stress in *S. pombe*

Introduction.

The endoplasmic reticulum (ER) is responsible for folding the vast majority of secretory and transmembrane proteins. ER protein folding homeostasis is monitored and maintained by the signaling pathway termed the unfolded protein response (UPR) (Walter and Ron, 2011). The most evolutionarily conserved branch of the UPR is the ER-transmembrane kinase/endoribonuclease Ire1. Direct binding of unfolded proteins to the Ire1 lumenal domain triggers its oligomerization, trans-autophosphorylation, and foci formation, which activate Ire1's cytosolic RNase domain (Gardner and Walter, 2011; Karagöz et al., 2017; Credle et al., 2005; Aragón et al., 2009; Korennykh et al., 2009). In *Schizosaccaromyces pombe*, activated Ire1 reduces the ER folding burden by cleaving a set of mRNAs encoding ER-targeted proteins. This Ire1-mediated cleavage leads to degradation of the mRNA substrates in a process termed regulated Ire1-dependent decay (RIDD) for all but one of its substrates (Hollien and Weissman, 2006; Kimmig and Diaz et al., 2012) (Figure 1.1A).

BIP1 mRNA, which encodes for the most abundant chaperone protein in the ER, is truncated by Ire1 in its 3'UTR during ER stress. *BIP1* mRNA was observed to run smaller on a gel during heat shock in *S. pombe* over 25 years ago (Pidoux and Armstrong, 1992) and was thereafter used as a phenotypic readout for ER stress (D'Alessio et al., 1999). The origin of the size change wasn't investigated until decades later when it was found to be a cleavage substrate of Ire1 (Kimmig and Diaz et al., 2012). Unlike all other substrates of Ire1, the 5' cleavage product of *BIP1* mRNA is not degraded. In fact, the half-life of truncated *BIP1* mRNA (*tBIP1*) is 70 minutes, significantly longer than the 20-minute half-life of the full-length mRNA. The fragment, which lacks a polyA tail but contains the complete coding sequence, accumulates to four times its normal level and is translated with equal efficiency to its full-length

counterpart. The mechanism behind *BIP1* mRNA's unique processing during ER stress in *S. pombe* is unknown.

Results and Discussion.

***Bip1* mRNA and RIDD substrates have distinct fates.**

The decay of RIDD 5' cleavage products is dependent on 3' to 5' mRNA degradation machinery called the exosome (Kimmig and Diaz et al., 2012) (Figure 1.1B). When *SKI2*, which encodes a helicase component of the cytosolic exosome, is knocked out, we found that *GAS2* mRNA, a RIDD substrate, is only transiently down-regulated during ER stress and returns to pre-stress levels by the one-hour time point (Figure 1.1C). In contrast, *BIP1* mRNA is efficiently truncated for the duration of the UPR in both WT and Δ*ski2* cells. Why the RIDD substrate is only briefly down-regulated but *BIP1* mRNA is persistently cleaved in the Δ*ski2* mutant strain is unknown. Ire1 may be prevented from accessing RIDD cleavage sites due to the critical accumulation of RNA fragments at the ER surface when they cannot be cleared by the exonuclease machinery in Δ*ski2* cells. A physical barrier restricting Ire1 cleavage of RIDD substrates does not explain how *BIP1* mRNA is consistently cleaved. The cleavage of *BIP1* mRNA and RIDD substrates may be spatially separated in distinct regions of the ER, possibly dependent on their initial ER-targeting. Ire1 has been shown *in vitro* to cleave *BIP1* cleavage site-derived hairpin RNAs significantly faster than RIDD substrate-derived hairpin RNAs (Li et al., 2018), so an alternative explanation is that Ire1's cleavage rate is moderately reduced in Δ*ski2* cells such that cleavage of RIDD substrates is no longer detectable but the activity is still sufficient to cleave the superior substrate *BIP1* mRNA. This substrate preference observed *in vitro* could be enhanced *in vivo* if Ire1's lumenal domain preferentially engages with the BiP1 nascent polypeptide chain through a higher affinity interaction. Another possible explanation that

is not mutually exclusive is that the RIDD substrate fragments competitively inhibit Ire1 cleavage by binding the Ire1 active site and the *BIP1* cleavage site is the only substrate with a high enough affinity for Ire1 to out-compete the accumulated fragments. In which case the affinity of Ire1 for *BIP1* mRNA dictates is preferential treatment rather than its cleavage rate. This possibility has not been explored.

We also observed that at later time points during sustained ER stress in WT cells, levels of total *BIP1* mRNA were reduced even though it was still predominantly in its more stable truncated form. Strikingly, levels of *GAS2* mRNA, a RIDD substrate, were increased during late-stage stress. The paradoxical down-regulation of *BIP1* mRNA and up-regulation of *GAS2* mRNA during sustained stress were amplified in Δ*ire1* and Δ*ski2* cells (Figure 1.1C). We considered that the cell may be modulating the levels of Ire1 substrates though transcriptional regulation in opposition to the consequences of Ire1-dependent cleavage so as to restore steady-state levels of the mRNAs after stress is resolved. To test if these changes in the transcriptome are specific to Ire1 substrates, we monitored levels of mRNAs that were known RIDD substrates (*IST2* and *SXA1*), ER-targeted mRNAs that were not RIDD substrates (*PKD1* and *ISP6*), and common reference genes that are not ER-targeted (*TBP1*, *ACT1*, *NDA2*). We measured levels of these mRNAs after 1, 5, and 20 hours of stress in WT and Δ*ire1* cells by real-time quantitative PCR (RT-qPCR) (Figure 1.1D). We found that the other RIDD substrates were not up-regulated in the same way as *GAS2* mRNA during late-stage stress. The ER-targeted mRNAs that were not RIDD substrates were both modestly up-regulated during stress in an Ire1-independent manner. Surprisingly, the control mRNAs (TATA Binding Protein, Actin, and α-Tubulin) were not static over the course of stress, even though these are transcripts commonly chosen as

reference genes due to the expectation that their expression does not change during stresses and other cellular perturbations.

Cell death programs have been known to cause global transcriptional changes (Mirza et al., 2003; Ren et al., 2008; Dong et al., 2017). To test if the wide-spread changes we observed in RNA level during sustained ER stress were due to cell death programs, we monitored the growth of liquid cultures of WT, Δ*ire1*, and Δ*ski2 S. pombe* strains and a strain with a mutation at the Ire1 cleavage-site of *BIP1* (ΔCTGGTG\C) over the course of ER stress (Figure 1.2A). All cell lines grew equally well without stress. Growth was initially arrested upon addition of 2 mM dithiothreitol (DTT), an ER stressor that reduces protein disulfide bonds, but after several hours, the WT, Δ*ski2*, and *BIP1* mutant strains recovered and grew in log phase to saturation. The Δ*ire1* strain also eventually recovered but took over a day longer. To test if the delayed recovery of the Δ*ire1* strain was due to cell death or a longer arrest phase, both stressed and unstressed cultures were serially diluted and plated in a spot assay on growth media (Figure 1.2B). Only the stressed Δ*ire1* sample had a growth defect of any kind, indicating these cells were less viable. Because the WT and Δ*ski2* strains grown with DTT didn't have a growth phenotype in the spot assay, we surmised that the changes we observed in RNA level in these strains was likely not due to apoptosis or other cell death programs.

Previous studies showed that Δ*ire1* and Δ*ski2* strains had similar growth defects during ER stress, demonstrated by spot assays on plates containing tunicamycin, a drug that induces ER stress by inhibiting N-linked glycosylation (Kimmig and Diaz et al., 2012). This led to the hypothesis that the dominant pathway by which Ire1 restored homeostasis was the degradation of ER-targeted mRNAs, since RIDD substrates are only transiently down-regulated in the Δ*ski2* strain. It was surprising, therefore, that the Δ*ski2* strain behaved like WT in our experiments. We

repeated the spot assay experiments with the four strains described above on plates containing an ER stressor (Figure 1.2C). As before, all the strains grew equally well on growth media, but on plates with 0.08 μg/mL tunicamycin, both the Δ*ire1* and Δ*ski2* strains failed to grow after two days. Given four days, however, the Δ*ski2* strain did show some growth, though it grew much more poorly than the WT strain, while the Δ*ire1* strain did not. The discrepancy in the growth of liquid versus solid cultures has been seen before for ER stress in *S. pombe* cells (Kimmig and Diaz et al., 2012) and suggests Ire1's multiple outputs could vary in level of importance with different growth conditions. It is important to note that the liquid cultures were stressed with DTT while the spot assays were plated on tunicamycin; the different stressors may contribute to the discrepancy in the growth phenotype. Growth of liquid cultures stressed with tunicamycin and growth of plated cells stressed with DTT have not been evaluated. The distinct growth phenotypes of the Δ*ire1* strain compared to the Δ*ski2* strain seen in liquid cultures may be due to the persistent *BIP1* mRNA cleavage in the Δ*ski2* strain. The accumulation of *BIP1* mRNA and, consequently, up-regulation of BiP1 protein could account for the improved survival of Δ*ski2* cells during stress. Additionally, the transient down-regulation of RIDD substrates at very early time-points during stress in the Δ*ski2* strain may be enough to restore homeostasis under certain conditions. We cannot rule out the existence of a yet unidentified output of Ire1 that contributes as well.

The *BIP1* 3'UTR and signal sequence are sufficient and required for cleavage and stabilization.

To test whether the *BIP1* 3'UTR is sufficient to produce a stable truncated transcript, we created a construct with an *NMT1* repressible promoter and 5'UTR, *BIP1* signal sequence, *GFP* coding sequence, and *BIP1* 3'UTR. We found that the chimeric construct was processed the

same way as the endogenous *BIP1* mRNA; it was cleaved in an Ire1-dependent manner and the truncated fragment was stable, indicating the *BIP1* 3'UTR and signal sequence are sufficient for cleavage and stabilization (Figure 1.3A). Additionally, the chimeric construct was cleaved after one hour of ER stress in Δ*ski2* cells at a time when processing of RIDD substrates is not detected. Because the chimera does not contain the BiP1 coding sequence, the preferential cleavage of the *BIP1* 3'UTR from both the endogenous mRNA and the chimera in Δ*ski2* cells must not depend on interactions between the BiP1 nascent chain and the Ire1 lumenal domain. It is still possible the continued activity of Ire1 on the *BIP1* cleavage site over RIDD substrates is due to the *BIP1* cleavage site being an inherently superior substrate for Ire1 or due to spatial separation at the ER membrane conferred by distinct targeting mechanisms, as the chimera does contain the *BIP1* signal sequence.

BIP1 is the only transcript that is stabilized after Ire1 cleavage and is also the only one to be cleaved in its 3'UTR; the RIDD substrates are all cleaved in their 5'UTR or coding sequences. The degradation of the 5' cleavage products of RIDD substrates is dependent on the recruitment of No-Go Decay (NGD) machinery (Guydosh and Kimmig et al., 2017). When translating ribosomes stall and stack up at the truncated end of the mRNA, NGD is initiated by endonucleolytic cleavage in the vicinity of the stalled ribosome. There is no known dedicated degradation mechanism for a substrate like *tBIP1* mRNA as no ribosomes would reach the cleavage site in the 3'UTR to recruit the NGD machinery. To test if the location of cleavage dictates the fate of the mRNA, we created another set of chimeric constructs. We used a synthetic mRNA containing the 5' and 3'UTRs of tubulin (*NDA2*) mRNA and the open reading frame of a *GAS2* mutant mRNA in which four known RIDD cleavage sites were mutated. Within the *NDA2* 3'UTR, we inserted a *HAC1*-derived RNA splicing cassette

optimized for *S. pombe* (Figure 1.3B). This construct has two Ire1 cleavage sites and has previously been shown to be efficiently spliced in *S. pombe* (Li et al., 2018). We mutated the two cleavage sites one at a time and tested the stability of the truncated RNAs. We found that both the full-length and truncated mRNAs were down-regulated upon stress in an Ire1- and Ski2-dependent manner (Figure 1.3C). Therefore, the chimeric mRNA behaved like a RIDD substrate. Because the GFP chimera containing a *BIP1* 3'UTR was stabilized after truncation but the modified splicing construct was not, the location of cleavage must not dictate the fate of the mRNA. Rather, there must be something in the *BIP1* 3'UTR that is lacking in the splicing construct that allows it to evade decay.

***BIP1* mRNA has structure in its 3'UTR that is rearranged after truncation.**

The increase of the *tBIP1* mRNA half-life after losing its polyA tail is confounding because polyA tails are generally linked to stability and translational efficiency (Chen et al., 2011; Preiss et al., 1998). However, there are a number of RNAs that serve as precedence for exceptions to this rule. Histone mRNAs terminate in a well-conserved 3' stem-loop structure that binds a stem-loop binding protein (SLBP) (Marzluff et al., 2008). SLBP functions like the polyA binding proteins found on most mRNAs by looping back to the 5' cap structure to enhance histone mRNA translation (Ling et al., 2002).

Recent biochemical interrogations of the long non-coding nuclear RNAs Malat1 and MENβ revealed that these RNAs stabilize their 3' end by folding into a triple helix structure with classic Watson-Crick base-pairing on one face and Hoogsteen base-pairing on the other (Brown et al, 2012; Wilusz et al., 2012). Multiple investigators tested the stability of the structures by putting them after the 3'UTR of cytosolic mRNAs (β-globin mRNA (Brown et al., 2012) or a chimeric GFP or mCherry mRNA (Wilusz et al., 2012)). Both of these synthetic transcripts were

stable and translated with equal efficiency as their polyadenylated counterparts-even though there was no evidence of any protein binding the 3' end to circularize the mRNA and boost translation.

Using these examples as inspiration, we sought to determine if *tBIP1* mRNA contained a structure in its 3'UTR that stabilized the end of the transcript in lieu of a polyA tail. Although computational modeling methods have been developed to predict RNA structure, these theoretical methods are limited and generally unable to accurately predict structures for RNA sequences longer than 100 residues (Ponce-Salvatierra et al., 2019; Magnus et al., 2014). To aid the modeling programs, we interrogated the structure of *BIP1* mRNA using both *in vitro* and *in vivo* biochemical techniques and used this data to apply constraints to the model. First, we performed Multiplexed -OH Cleavage Analysis (MOHCA-seq) on both the truncated and full-length *BIP1* 3'UTRs (Cheng et al, 2015). MOHCA-seq creates nucleotide-resolution proximity maps that represents three-dimensional RNA structure *in vitro* through generation of hydroxyl radicals from sources that are randomly incorporated into the RNA backbone. These radicals cause localized strand scissions that are spatially correlated with the radical source. Determining the sequence positions of the 5'- and 3'-ends of the resulting RNA fragments provides pairwise proximity information, which can be used with computational modeling to resolve 3D structures in the RNA.

The proximity map of the truncated and full-length 3'UTRs revealed a number of structural features that both RNAs shared (Figures 1.4A and 1.4B). Three stem-loops were evident in both datasets: the first beginning 10 bases after the stop codon with the middle of the loop at around 40 bases, the second beginning 90 bases after the stop codon with a loop at 125 bases, and the third beginning 150 bases after the stop codon with a loop at 225 bases. The full-

length 3'UTR contained an additional stem-loop that started 300 bases after the stop codon with the loop at around 370 bases. Ire1 cleaves *BIP1* mRNA after base 373, so the cleavage site likely resides at the tip of this long stem-loop. The truncated 3'UTR showed evidence of a small hairpin structure starting 280 bases after the stop codon with the loop at 310 bases. The proximity map for the truncated RNA also showed scattered interactions between the last 70 bases before the cleavage site and sequence far upstream. These were not discreet interactions with hot spots of proximity. The scattered pattern of this data suggested that the RNA may fold into a population of structures or that the interactions between the end of the RNA and upstream structure are dynamic.

The MOHCA-seq data showed the location of large RNA structures but did not provide information on what bases were paired to each other. Additionally, the structure *BIP1* RNA folds into *in vitro* may not reflect its structure *in vivo* where the presence of RNA binding proteins and chaperones may influence the folding of the mRNA. To complement the *in vitro* data we collected, we next analyzed DMS-seq data (Rouskin et al., 2014) from previous studies (Li et al., 2018) to ascertain what nucleotides are base-paired or free *in vivo*. *S. pombe* cultures were grown with and without an ER stressor in the presence of dimethyl-sulfide (DMS), which modifies unbase-paired adenines and cytosines. Determining the sequence positions of modified bases yields information on the base-pairing status of each nucleotide. The modification profiles of *BIP1* mRNA from the stressed and unstressed samples were similar for most of the transcript. However, the last 50-60 bases leading up to the cleavage site showed significant modification differences, indicating changes in the base-pairing status of these nucleotides that could be caused by structural rearrangements. The data from the *in vitro* MOHCA-seq experiments and *in vivo* DMS-seq experiments both show that the full-length and truncated *BIP1*

have similar structural features for the first 300 bases of the 3'UTR and structural changes or rearrangements after that, validating both methods.

We used the MOHCA-seq and DMS-seq data to constrain computational modeling of the *BIP1* 3'UTR. Additionally, we took into account possible evolutionary conservation. Aligning the *BIP1* 3'UTR from other species of the *Schizosaccaromyces* genus shows that the Ire1 cleavage site is conserved in at least two other species: *S. octosporus* and *S. cryophilus* (Figure 1.4C). Although the sequence of the rest of the 3'UTR is not as well conserved as the cleavage site, structural elements could be conserved even where the sequence varies. We used an online tool called LocARNA to predict a consensus structure around the *BIP1* cleavage site. LocARNA is a tool from the Vienna RNA package that simultaneously folds and aligns multiple input sequences to output a structure all sequences can fold into (Will et al., 2007; Will et al., 2012; Raden et al., 2018). We used the 3'UTR sequences of *BIP1* mRNA from *S. pombe*, *S. octosporus,* and *S. cryophius* as our input sequences and constrained the modeling with the MOHCA-seq and DMS-seq data. The structure predicted for the hairpin around the cleavage site was very energetically favorable and agreed with the DMS-seq data well. Additionally, the conserved structure placed the cleavage site within a 9-mer loop at the tip of the hairpin. The cleavage sites of well-characterized substrates of Ire1 from across eukaryotes are all located in the loops of hairpin RNAs (Gonzalez et al., 1999; Yoshida et al., 2001; Calfon et al., 2002; Gaddam et al., 2012; Moore and Hollien, 2015), further validating the existence of this structure. The LocARNA program was unable to predict favorable structures for the sequences from all species further upstream of the cleavage site when constraints based on experimental data were included, indicating that the conservation of structure around the cleavage site may not extend that far upstream. We used mfold, another computational RNA modeling program that

uses a single RNA sequence as input (Zuker, 2003), to predict the structure of the rest of the RNA within experimental constraints (Figure 1.4D).

The long stem-loop around the cleavage site is significantly larger and more energetically stable than hairpin cleavage sites found in other Ire1 substrates. Additionally, being located in the 3'UTR, the structure is not continually disrupted by translating ribosomes like hairpins located in the coding sequence or 5'UTR might be (Moore and Hollien, 2015). The length and stability of the stem-loop could contribute to the persistent cleavage of *BIP1* mRNA during stress in Δ*ski2* cells when Ire1 fails to cleave RIDD substrates due to either over-crowding or competitive inhibition by stabilized fragments of RIDD substrates. The modeling predicted two short hairpins at the end of the *tBIP1* 3'UTR, but this section did not include constraints from DMS-seq experiments (reads shorter than twenty bases cannot be reliably mapped back to the genome, so there isn't DMS-seq data for the end *tBIP1* mRNA). MOHCA-seq data suggested that the tail of the truncated RNA may wrap around to interact with upstream sequence. These interactions could involve base-pairing between the end of the mRNA and the loops of upstream hairpins, forming structures called pseudoknots. The modeling programs were not sophisticated enough to predict these kinds of complex long-range interactions.

Deletions in the *BIP1* 3'UTR do not destabilize the truncated product

To test how much each portion of the structure in the 3'UTR contributes to the stability of *tBIP1* mRNA, we created a series of mutants in the endogenous *BIP1* gene in which we cut out progressively larger portions of the 3'UTR beginning just after the stop codon. The barriers of the deletions were chosen based on the structural elements we identified in the 3'UTR so each mutant deletes one additional major structural element (Figure 1.5, upper image). We found that steady-state levels of the full-length *BIP1* mutant mRNAs were variable in unstressed cells; as

the size of the deletion increased, the amount of mRNA increased (Figure 1.5, lower image). After one hour of stress with 2 mM DTT, all of the mutant mRNAs were efficiently cleaved, but each construct accumulated to different extents after truncation. The mutants with larger deletions that were more abundant before stress did not have as much fold enrichment of the truncated product. Interestingly, although levels of mutant full-length *BIP1* mRNA were variable before cleavage, the levels of *tBIP1* mRNA were relatively equal from mutant to mutant after truncation. The reduced abundance of mRNAs with larger deletions could be caused by destabilization of the mRNA due to the deletion of a sequence or structure that interacts with and stabilizes the truncated 3' end or serves as a protein binding site. Because the expression levels of the mutant *BIP1* mRNAs vary so widely before cleavage but are approximately equal after cleavage, it is also possible that there exists some limiting factor that can only stabilize a certain amount of truncated transcripts.

Conclusions.

The improved survival of the Δ*ski2* strain over ΔIre1 in liquid culture in the presence of DTT suggests the role of the stabilized *tBIP1* mRNA may be more significant than previously estimated. The importance of *BIP1* mRNA cleavage and stabilization is underscored by the conservation of the cleavage site in other *Schizosaccharomyces* species and that it is the most efficiently cleaved Ire1 substrate tested *in vitro* (Li et al., 2018). In other species, the BiP1 chaperone protein is up-regulated transcriptionally and serves an essential role in the survival of ER stress (Mori et al., 1996; Yoshida et al., 2000), so it is not altogether surprising that *S. pombe*, in which no UPR transcriptional program has been characterized, has evolved a robust transcription-independent way to up-regulate the protein. The mechanism behind the persistent cleavage of *BIP1* mRNA in the Δ*ski2* strain remains an open question and further experiments

should be done to test the role of mRNA targeting *in vivo* and to compare the affinity of Ire1 RNA substrates for the enzyme *in vitro*. The long stem-loop structure in which the *BIP1* cleavage site resides could contribute to its preferential cleavage. The stem-loop may be able to reach sites of Ire1 activity that are otherwise occluded by undigested 5' RIDD fragments. The structure is made up of 125 bases, which is up to one hundred bases more than other typical Ire1 substrates. Coupled with its location in the 3'UTR where it would not be disrupted by translating ribosomes, this structure is significantly more stable than the much shorter stem-loops found around RIDD substrate cleavage sites.

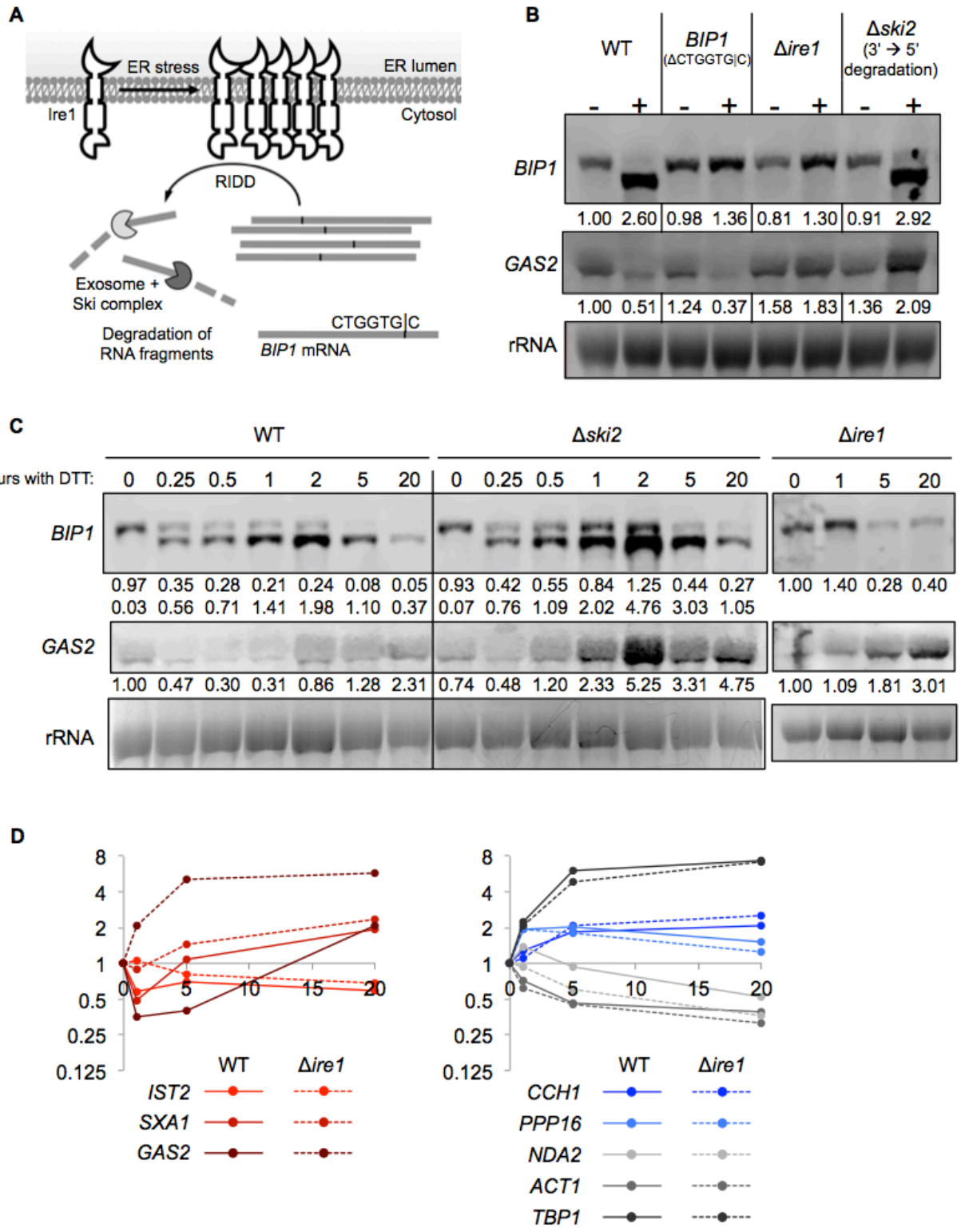
A
ER stress
ER lumen
Ire1
Cytosol
RIDD
Exosome +
Ski complex
Degradation of
RNA fragments
CTGGTG|C
BIP1 mRNA
B
WT
BIP1
(ΔCTGGTG|C)
Δire1
Δski2
(3' → 5'
degradation)
- + - + - + - +
BIP1
1.00 2.60 0.98 1.36 0.81 1.30 0.91 2.92
GAS2
1.00 0.51 1.24 0.37 1.58 1.83 1.36 2.09
rRNA
C
WT
Δski2
Δire1
Hours with DTT: 0 0.25 0.5 1 2 5 20 0 0.25 0.5 1 2 5 20 0 1 5 20
BIP1
0.97 0.35 0.28 0.21 0.24 0.08 0.05 0.93 0.42 0.55 0.84 1.25 0.44 0.27 1.00 1.40 0.28 0.40
0.03 0.56 0.71 1.41 1.98 1.10 0.37 0.07 0.76 1.09 2.02 4.76 3.03 1.05
GAS2
1.00 0.47 0.30 0.31 0.86 1.28 2.31 0.74 0.48 1.20 2.33 5.25 3.31 4.75 1.00 1.09 1.81 3.01
rRNA
D
8
4
2
1
0.5
0.25
0.125
0 5 10 15 20
WT Δire1
IST2
SXA1
GAS2
CCH1
PPP16
NDA2
ACT1
TBP1

Figure 1.1. *BIP1* mRNA and RIDD substrates have distinct fates during ER stress. (**A**) Schematic of the Unfolded Protein Response in *S. pombe* cells. Upon ER stress, activated Ire1 cleaves a subset of ER-targeted mRNAs. These cleavage products are substrates for degradation by the 5'→3' exonuclease Xrn1 and the 3'→5' exosome with accessory proteins, including Ski2, a component of the helicase. *BIP1* mRNA is cleaved at the sequence CTGGTG|C (where "|" denotes the cleavage site) and escapes degradation. (**B**) Northern Blot with biotinylated probes against *BIP1* and *GAS2* coding sequences from WT, *BIP1* cleavage mutant ΔCTGGTG|C, Δ*ire1*, and Δ*ski2 S. pombe* strains grown with and without 2 mM DTT for 1 hr. Ethidium bromide staining of 18S rRNA shown as loading control. (**C**) Northern Blot as described above with time points at 0.25, 0.5, 1, 2, 5, and 20 hours after DTT addition for WT and Δ*ski2* strains and 1, 5, and 20 hours for Δ*ire1* strain. (**D**) Real-time quantitative polymerase chain reaction for known RIDD substrates (*GAS2, SXA1, IST2*) in red, ER-targeted mRNAs that haven't been identified as RIDD substrates (*CCH1, PPP16*) in blue, and house keeping genes (*TBP1, ACT1, NDA2*) in grey in WT (solid lines) and Δ*ire1* (dashed lines) strains after 1, 5, and 20 hours of stress with 2 mM DTT.

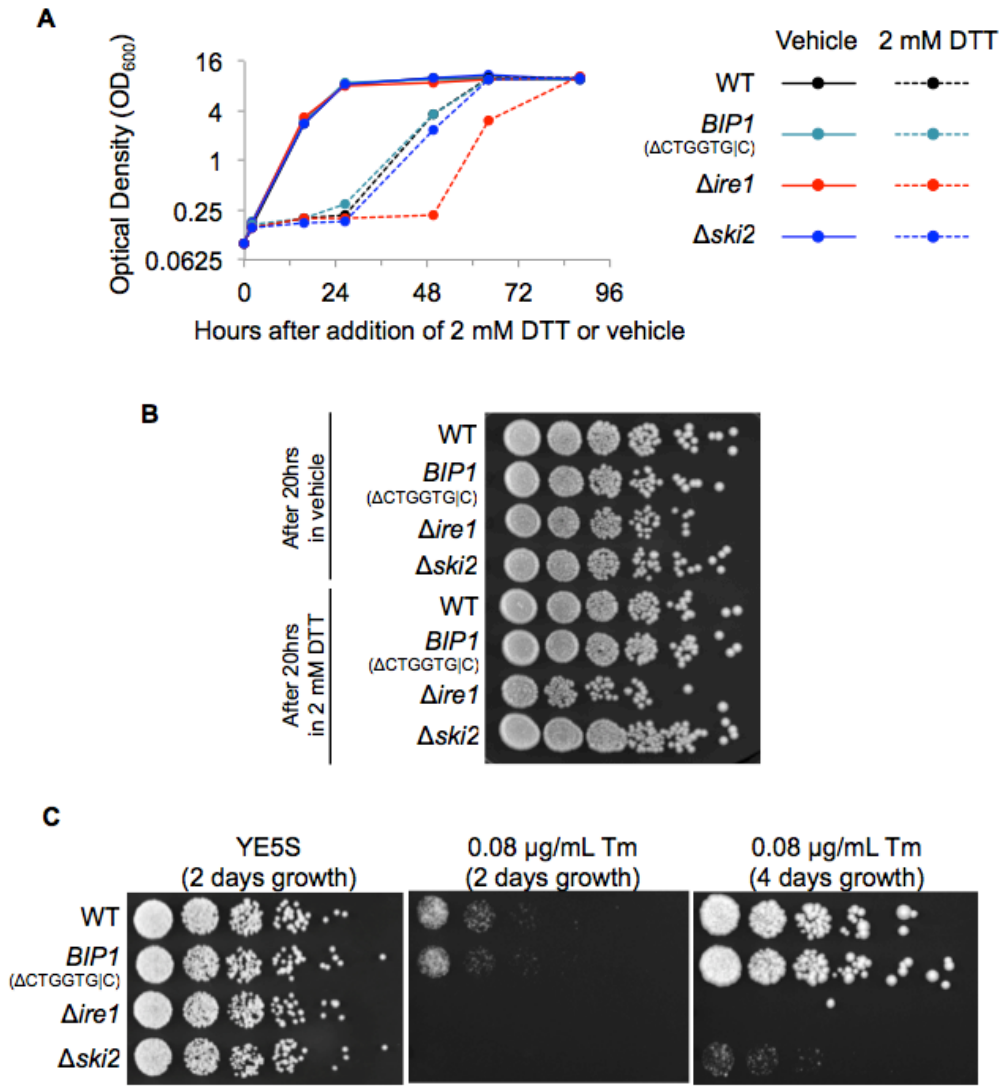

Figure 1.2. Δ*ire1* has a growth phenotype during ER stress.
(**A**) Liquid growth assay of the strains described in figure 1.1. OD_{600} measurements taken over time as cells grew with either 2 mM DTT or vehicle. (**B**) Spot assay of serial 5-fold dilutions after 20 hr growth with vehicle or 2 mM DTT. Cells washed three times before plating on YE5S growth media. (**C**) Spot assay on YE5S plates with and without 0.08 µg/mL tunicamycin. Imaged 2 or 4 days after plating.

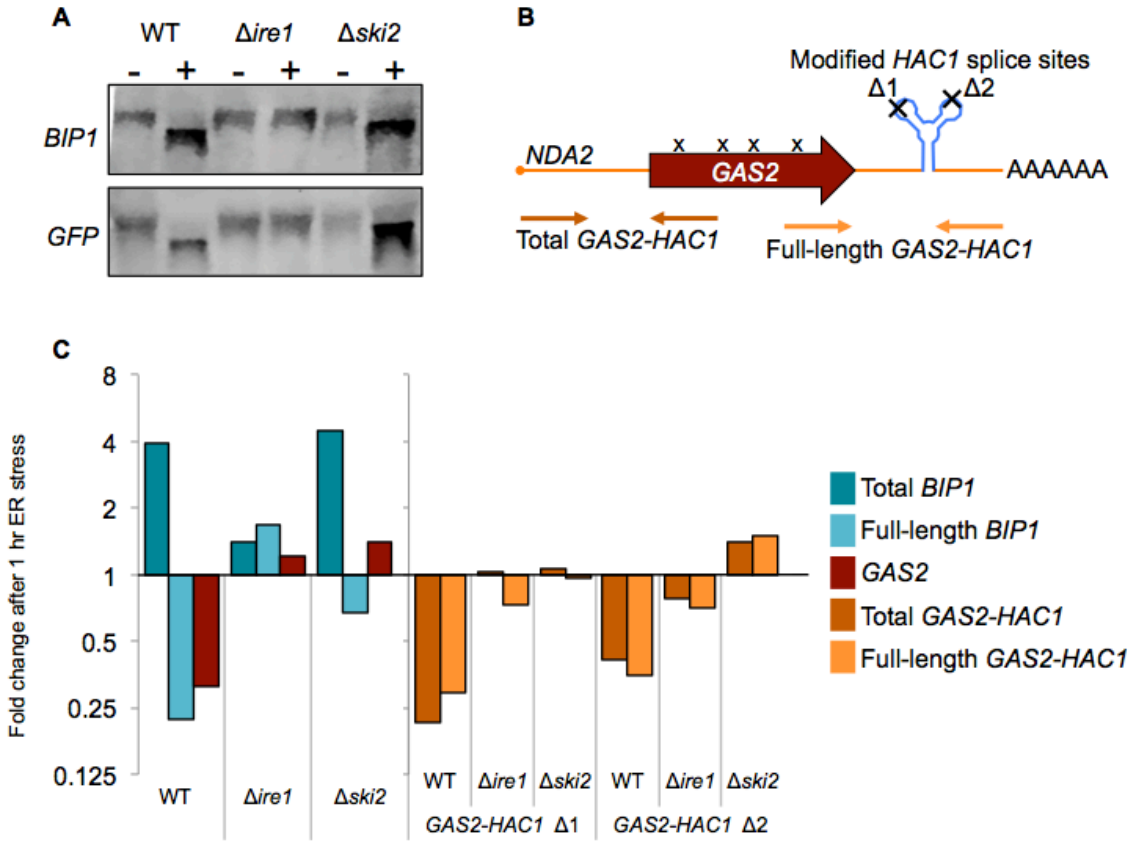

Figure 1.3. Chimeric mRNAs cleaved in their 3' untranslated regions require the *BIP1* 3'UTR to be stable after cleavage.

(**A**) Northern Blot with biotinylated probes for *BIP1* and *GFP* coding sequences in WT, Δ*ire1*, and Δ*ski2* strains. (**B**) Diagram of *GAS2-HAC1* chimera. mRNA contains the *NDA2* 5' and 3' UTRs, *GAS2* signal sequence and CDS with mutations at 4 known RIDD cleavage sites, and modified *HAC1* splice sites in the 3'UTR. One branch's cleavage site is mutated in each construct so only one functional cleavage site remains in each. (**C**) RT-qPCR of total *BIP1,* full-length *BIP1*, *GAS2*, and the two *GAS2-HAC1* chimeras in WT, Δ*ire1,* and Δ*ski2* strains. Shown is fold change after 1 hr ER stress with 2 mM DTT.

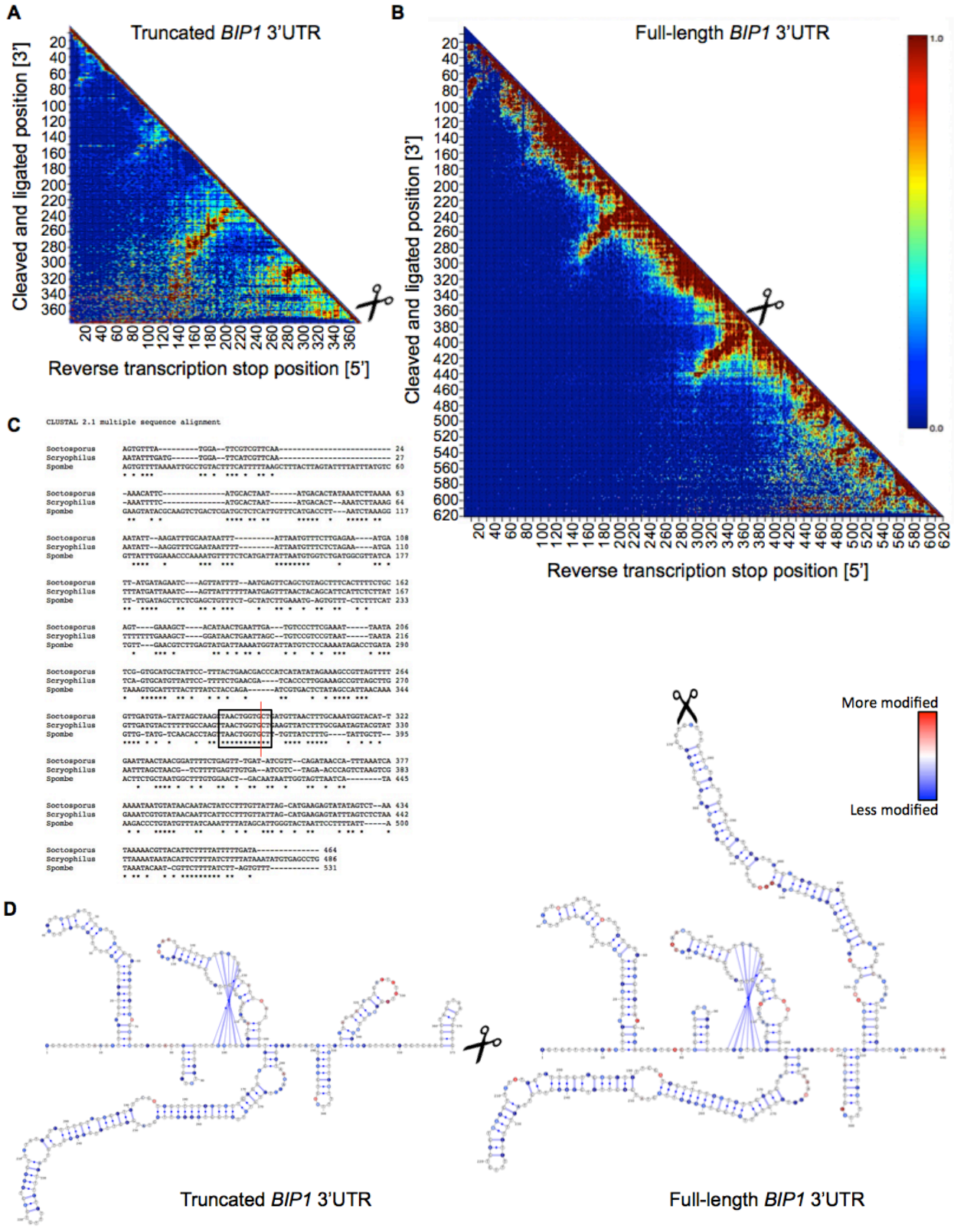
A
Truncated BIP1 3'UTR
Cleaved and ligated position [3']
Reverse transcription stop position [5']
B
Full-length BIP1 3'UTR
Cleaved and ligated position [3']
Reverse transcription stop position [5']
1.0
0.0
C
CLUSTAL 2.1 multiple sequence alignment
Soctosporus
Scryophilus
Spombe
D
More modified
Less modified
Truncated BIP1 3'UTR
Full-length BIP1 3'UTR

Figure 1.4. Structure of truncated and full-length *BIP1* mRNA.

MOHCA-seq data for truncated *BIP1* 3'UTR (**A**) and full-length *BIP1* 3'UTR (**B**). Data are represented on a proximity map based on the frequency of any combination of residues being the 5' (x-axis) or 3' (y-axis) ends of the RNA fragments. Location of Ire1 cleavage site is indicated by scissors icon. (**C**) Clustal omega alignment of predicted *BIP1* 3'UTR from *S. pombe*, *S. cryophilus*, and *S. octosporus*. Significant conservation around the Ire1 cleavage site (indicated by red line) is shown in the black box. (**D**) Structure of truncated and full-length *BIP1* 3'UTR. Each adenine and cytosine is color-coded based on extent of DMS modification. Red is more modified and less likely to be base-paired. Blue is less modified and more likely to be base-paired. High resolution versions of (C) and (D) are included in additional files.

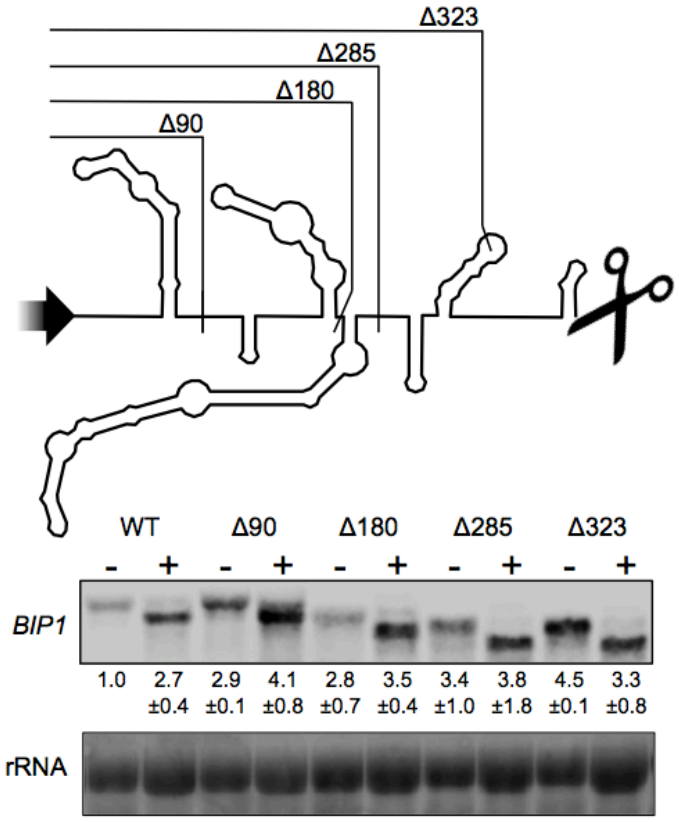

Figure 1.5. Deleting structural features from the *BIP1* 3'UTR.
On top: Diagram of *BIP1* truncated 3'UTR. In each mutant, a portion of the 3'UTR was deleted from the stop codon to the indicated site. Below: Northern Blot with biotinylated probe for indicated mutant *BIP1* mRNAs with and without 1 hr 2 mM DTT.

Table 1.1. qPCR primers

qPCR primers description	Sequence
BIP1 CDS Forward	CTGACTCGATGCTCTCATTGTT
Total *BIP1* mRNA Reverse	GGCTATAGAGTCACGATTCTGGTAG
Full-length *BIP1* mRNA Reverse	CAGTTCCACAAAGCCATTAGC
GAS2 5' UTR Forward	GCGTTAAGAGGATTTACACATCGACGG
GAS2 5' UTR Reverse	GGAATGTGTTGGGCAAGAGAGAAATGAATC
NDA2 CDS Forward	CTATCACCGCTTCTCTTCG
NDA2 CDS Reverse	GTGGATCACATTTTACCATTTG
IST2 Forward	GGTGCTTTTTTTATTCAATTTTGG
IST2 Reverse	GATCTCAGGATGCATCCTGCTTTTCTTG
SXA1 Forward	CAATATGATCATGTGGCGAGG
SXA1 Reverse	CCGAGATTTGGAGTGACACCG
CCH1 Forward	CAGTTATCAGCAAGTAAGCTC
CCH1 Reverse	CATACTTTAACCGGAGAGGCTC
PPP16 Forward	CACGGCAAATCAAACAAAGCGC
PPP16 Reverse	GTTAAGGGACCTTCAAATGTTC
ACT1 Forward	CTGGTATCGTCTTGGACTCTGG
ACT1 Reverse	CTTCAAACTGCTGCTCAATCTTC
TBP1 Forward	CCGAGGATGACTCCAAGCTC
TBP1 Reverse	GCACCAGTTAAAACAATTTTACCAG
Full-length *GAS2-HAC1* mRNA Forward	CATGGTGCCGATTCTTGTAGCTGG
Full-length *GAS2-HAC1* mRNA Reverse	CTGGTGGTTTATTTGCAAAGATAGAGTGGATTAG
Total *GAS2-HAC1* mRNA Forward	GTGTAGCGCGTTTAGTTGCATTTACATTC
Total *GAS2-HAC1* mRNA Reverse	GCCCAAGTTGGAAATGATCTTAGCATCTTC

Table 1.2. Primers for Northern Blot probes

Primer description	Sequence
BIP1 CDS Forward	GCTGAAGCTTACCTCGGAAAGCCTG
BIP1 CDS Reverse	CCATGTTAATCTCCTCGAACTTAGCACGGG
GAS2 CDS Forward	CCAAATTTACTTTGCAGCTGTTGTCGGC
GAS2 CDS Reverse	GGCAGCACGAACGTAAGCG
GFP CDS Forward	GTGAAGAATTATTCACTGGTGTTGTCCCAATTTTGG
GFP CDS Reverse	CGCTTCCATCTTCAATGTTGTGTCTAATTTTGAAGTTAAC

Materials and Methods.

Strains, plasmids and growth conditions

Standard growth conditions, cloning methods, and transformation methods for *S. pombe* were used (Guthrie and Fink, 2002). Reporter constructs were integrated at *URA4* or *LEU1* loci. Mutant alleles were integrated at the endogenous locus of the gene.

To collect stressed yeast samples, overnight cultures were diluted to an OD_{600} of 0.15 and allowed to grow to an OD of 0.3-0.6. 10 mL of the culture was harvested for the time zero sample and DTT was added to the rest of the culture to a final concentration of 2 mM and harvested after specified durations of growth.

RNA Analysis

Total RNA was purified from yeast cultures using phenol extraction (Köhrer and Domdey, 1991). Total RNA samples extracted from cells were diluted to 3-5 μg/μL and the concentration was checked three times on a 1:10 dilution of each sample. Quality of rRNA was checked on agarose gel with SYBR Gold staining. 10 μg of RNA was mixed with 1.33x Loading Buffer (65% Formamide, 8% Formaldehyde, trace EtBr and Bromophenol Blue), heated to 80°C, and put directly on ice.

To make the gel, 5.1 g of agarose was melted in 243 mL of water, then allowed to cool to 50°C when 34 mL of 10x E buffer and 61.5 mL filtered 37% formaldehyde were added. The mixture was poured into a gel mold that was thoroughly cleaned with RNase Zap, rinsed, dried, and leveled. RNA samples were loaded and run in 1x E buffer for 8 hrs at 90 V. The running buffer was mixed every 2 hrs to prevent a pH gradient from forming. We imaged the gel before the transfer with EtBr to use 18S rRNA as our loading control.

We transferred the gel to a positively charged membrane (Life Technologies AM10102) by draping two long pieces of Whatman paper over a glass plate so the ends soaked in a tray of 10x SSC. We placed the gel upside-down on the soaking Whatman papers and placed the membrane, cut to size, on top. Three pieces of dry Whatman paper were stacked on top of the membrane followed by ~6 inches of paper towels, a glass plate, and a small weight or textbook. The transfer tower was leveled and left to transfer by capillary action overnight (~12-16 hrs). The membrane was imaged with EtBr to check for an even transfer, then the membrane was dried and the RNA was crosslinked to the membrane with Strata crosslinker set to "Autocrosslink" twice.

The membranes were pre-hybridized in hybridization buffer (Ambion ULTRAhyb-Oligo buffer—Life Technologies AM8663) at 42°C for 1 hr in a rotating tube. Biotinylated probes for Northern Blots were synthesized by PCR using cDNA or plasmid DNA as a template in the presence of 0.1 mM Biotin-16-UTP. Unincorporated biotinylated nucleotide was removed with PCR Clean-up kit (Macherey-nagel). The probe was boiled for 5 min, then put directly on ice. We mixed probe with fresh hybridization buffer and membranes were hybridized with probe by rotation overnight at 42°C.

The membrane was washed twice with 2x SSC and 0.1% SDS for 5 min at room temp, and then washed twice with 0.1x SSC and 0.1% SDS for 15 min at 50°C. The membranes were moved from the rotating tubes to black LiCor boxes. We blocked the membranes with 50% Odyssey Blocking Buffer with 1% SDS at room temp for 1 hr. We incubated the membrane with Streptavidin IR Dye (LICOR Biosciences 926-32230) diluted 1:10,000 in 50% Odyssey Blocking Buffer with 1% SDS for 30 min at room temp. The membrane was washed three times

with PBST and once with PBS for 5 min each. We scanned the membrane on an Odyssey LiCor with the 800 channel for 10 minutes.

For qPCR assays, cDNA was synthesized by reverse transcription using random hexamer DNA primers and VILO SuperScript kit (Thermo Fisher Scientific). PCR amplification was detected by SYBR Green and α-tubulin (*NDA2*) was used as a reference gene. For Figure 1.1D, three typical reference genes were measured (*TBP1*-TATA Binding Protein; *ACT1*-Actin; *NDA2*-α-tubulin) and we found that all three changed over long periods of ER stress. In this experiment, the average C_q of all mRNAs measured for each time point was used as reference.

Growth assay

For liquid cultures, overnight cultures were diluted to an OD_{600} of 0.1, grown to an OD of 0.3-0.6, and then diluted again to 0.1, when 2 mM DTT was added. Aliquots of the cultures were taken at indicated time points for OD_{600} measurement.

5-fold serial dilutions of *S. pombe* cells from liquid cultures at OD 0.3-0.6 were spotted on YE5S plates with or without 0.08 μg/mL tunicamycin. For Figure 1.2B, liquid cultures were washed with YE5S media three times before OD measurement and plating. Plates were photographed after 2-4 days growth at 30°C.

MOHCA-seq

MOHCA-seq was performed and analyzed as described (Cheng et al., 2015). The truncated *BIP1* 3'UTR (373 residues) and full-length *BIP1* 3'UTR (626 residues) were *in vitro* transcribed in the presence of 2'-NH_2-2'-dATP, which was randomly incorporated into the RNA sequence. After the modified base was coupled with isothiocyanobenzyl-Fe(III)•EDTA, the RNAs were folded. Addition of ascorbate activated the Fenton reaction at the backbone-tethered Fe(III) atoms which fragmented the RNA. A DNA adapter was ligated to the 3'-ends of the

resulting fragments to allow a reverse transcription reaction that terminated at the radical source. The resulting cDNA fragments were sequenced on a standard Illumina platform. MAPseeker software analysis quantified the data and generated a pairwise proximity map.

RNA structure prediction

The bases predicted by MOHCA-seq data to be involved in the stem-loop around the *BIP1* Ire1 cleavage site (300-440 in *S. pombe*, 215-365 in *S. octosporus*, and 225-370 in *S. cryophilus*, counting from after the termination codon) were inputted into the LocARNA program. Bases 1-90, 90-165, and 160-290 were individually used as inputs for the mfold program. DMS-seq data was used to restrict modeling by restraining bases modified by 70% or more than the most modified base in each window as "unbase-paired." The predicted structures were concatenated together.

References.

Aragón, T., van Anken, E., Pincus, D., Serafimova, I. M., Korennykh, A. V., Rubio, C. A., & Walter, P. (2009). Messenger RNA targeting to endoplasmic reticulum stress signaling sites. *Nature*. *457*(5), 736-741.

Brown, J. A., Valenstein, M. L., Yario, T. A., Tycowski, K. T. & Steitz, J. A. (2012). Formation of triple-helical structures by the 3'-end sequences of MALAT1 and MENβ noncoding RNAs. *Proceedings of the National Academy of Sciences*. *109*(47), 19202-19207.

Calfon, M., Zeng, H., Urano, F., Till, J. H., Hubbard, S. R., Harding, H. P., Clark, S. G., & Ron, D. (2002). IRE1 couples endoplasmic reticulum load to secretory capacity by processing the *XBP-1* mRNA. *Nature*. 415, 92-96.

Chen, C. A. & Shyu, A. (2011). Mechanisms of deadenylation-dependent decay. *Wiley Interdiscip Rev RNA*. *2*(2), 167-183.

Cheng, C. Y., Chou, F., Kladwang, W., Tian, S., Cordero, P., & Das, R. (2015). Consistent global structures of complex RNA states through multidimensional chemical mapping. *eLife*. e07600.

Credle, J. J., Finer-Moore, J. S., Pap, F. R., Stroud, R. M., & Walter, P. (2005). On the mechanism of sensing unfolded protein in the endoplasmic reticulum. *Proceedings of the National Academy of Sciences*. *102*(52), 18773-18784.

D'Alessio, C., Fernández, F., Trombetta, E. S., & Parodi, A. J. (1999). Genetic evidence for the heterodimeric structure of glucosidase II: The effect of disrupting the subunit-encoding genes on glycoprotein folding. *The Journal of Biological Chemistry. 274*(36). 25899-25905.

Dong, Y., Hu, J., Fan, L., & Chen, Q. (2017). RNA-seq-based transcriptomic and metabolomic analysis reveal stress responses and programmed cell death induced by acetic acid in *Saccharomyces cerevisiae*. *Scientific Reports*. 10.1038/srep42659.

Gaddam, D., Stevens, N., & Hollien, J. (2012). Comparison of mRNA localization and regulation during endoplasmic reticulum stress in *Drosophila* cells. *Molecular Biology of the Cell*. 24, 14-20.

Gardner, B. M. & Walter, P. (2011). Unfolded proteins are Ire1-activating ligands that directly induce the unfolded protein response. *Science*. 333, 1891-1894.

Gonzalez, T. N., Sidrauski, C., Dörfler, S., & Walter, P. (1999). Mechanism of non-spliceosomal mRNA splicing in the unfolded protein response pathway. *The EMBO Journal*. *18*(11), 3119-3132.

Guthrie, C. & Fink, G. R. (2002). Guide to yeast genetics and molecular and cell biology, Part C. *Methods in Enzymology*. 351.

Guydosh, N. R., Kimmig, P., Walter, P., & Green, R. (2017). Regulated Ire1-dependent mRNA decay requires no-go mRNA degradation to maintain endoplasmic reticulum homeostasis in *S. pombe*. *eLife*. e29216.

Hollien, J. & Weissman, J. S. (2006). Decay of endoplasmic reticulum-localized mRNAs during the unfolded protein response. *Science*. 313, 104-107.

Karagöz, G. E., Acosta-Alvear, D., Nguyen, N. T., Lee, C. P., Chu, F., & Walter P. (2017). An unfolded protein-induced conformational switch activates mammalian IRE1. *eLife*. e30700.

Kimmig, P., Diaz, M., Zheng, J., Williams, C. C., Lang, A., Aragón, T., Li, H., & Walter, P. (2012). The unfolded protein response in fission yeast modulates stability of select mRNAs to maintain protein homeostasis. *eLife*. e00048.

Köhrer, K. & Domdey, H. (1991). Preparation of high molecular weight RNA. *Methods in Enzymology*. 194, 398-405.

Korennykh, A. V., Egea, P. F., Korostelev, A. A., Finer-Moore, J., Zhang, C., Shokat, K. M., Stroud, R. M., & Walter, P. (2009). The unfolded protein response signals through high-order assembly of Ire1. *Nature*. 457, 687-693.

Li, W., Okreglak, V., Peschek, J., Kimmig, P., Zubradt, M., Weissman, J. S., & Walter, P. (2018). Engineering ER-stress dependent non-conventional mRNA splicing. *eLife*. e35388.

Ling, J., Morley, S. J., Pain, V. M., Marzluff, W. F., & Gallie, D. R. (2002). The histone 3'-terminal stem-loop-binding protein enhances translation through a functional and physical interaction with eukaryotic initiation factor 4G (eIF4G) and eIF3. *Molecular and Cellular Biology*. *22*(22), 7853-7867.

Magnus, M., Matelska, D., Łach, G., Chojnowski, G., Boniecki, M. J., Purta, E., Dawson, W., Dunin-Horkawicz, S., & Bujnicki, J. M. (2014). Computational modeling of RNA 3D structures with the aid of experimental restraints. *RNA Biology*. *11*(5), 522-536.

Marzluff, W. F., Wagner, E. J., & Duronio, R. J. (2008). Metabolism and regulation of canonical histone mRNAs: life without a poly(A) tail. *Nature Reviews Genetics*. *9*(11), 843-54.

Mirza, A., Wu, Q., Wang, L., McClanahan, T., Bishop, W. R., Gheyas, F., Ding, W., Hutchins, B., Hockenberry, T., Kirschmeier, P., Greene, J. R., & Liu, S. (2003). Global

transcriptional program of p53 target genes during the process of apoptosis and cell cycle progression. *Oncogene*. 22, 3645-3654.

Moore, K. & Hollien, J. (2015). Ire1-mediated decay in mammalian cells relies on mRNA sequence, structure, and translational status. *Molecular Biology of the Cell*. 26, 2873-2884.

Mori, K., Kawahara, T., Yoshida, H., Yanagi, H., & Yura, T. (1996). Signaling from endoplasmic reticulum to nucleus: transcription factor with a basic-leucine zipper motif is required for the unfolded protein-response pathway. *Genes to Cells*. 1, 803-817.

Pidoux, A. L. & Armstrong, J., (1992). Analysis of the BiP gene and identification of an ER retention signal in *Schizosaccharomyces pombe*. *The EMBO Journal*. *11*(4), 1583-1591.

Ponce-Salvatierra, A., Astha, Merdas, K., Nithin, C., Ghosh, P., Mukherjee, S., & Bujnicki, J. M. (2019). Computational modeling of RNA 3D structure based on experimental data. *Bioscience Reports*. 39, 10.1042/BSR20180430.

Preiss, T., Muckenthaler, M., & Hentze, M. W. (1998). Poly(A)-tail-promoted translation in yeast: Implications for translational control. *RNA*. 4, 1321-1331.

Raden, M., Ali, S. M., Alkhnbashi, O. S., Busch, A., Costa, F., Davis, J. A., Eggenhofer, F., Gelhausen, R., Miladi, J., Richter, A. S., Will, S., Wolff, J., Wright, P. R., & Backofen, R. (2018). Freiburg RNA tools: A central online resource for RNA-focused research and teaching. *Nucleic Acids Research*. 46, W25-W29.

Ren, Q., Yang, H., Gao, B., & Zhang, Z. (2008). Global transcriptional analysis of yeast cell death induced by mutation of sister chromatid cohesin. *Comparative and Functional Genomics*. 10.1155/2008/634283.

Rouskin, S., Zubradt, M., Washietl, S., Kellis, M., & Weissman, J. S. (2014). Genome-wide probing of RNA structure reveals active unfolding of mRNA structures *in vivo*. *Nature*. 505, 701-705.

Ruegsegger, U., Leber, J. H., & Walter, P. (2001) Block of Hac1 mRNA translation by long-range base pairing is released by cytoplasmic splicing upon induction of the unfolded protein response. *Cell*. 107, 103-114.

Walter, P. & Ron, D. (2011). The unfolded protein response: from stress pathway to homeostatic regulation. *Science*. 334, 1081-1086.

Will, S., Joshi, T., Hofacker, I. L., Stadler, P. F., & Backofen, R. (2012). LocARNA-P: Accurate boundary prediction and improved detection of structural RNAs. *RNA*. *18*(5). 900-914.

Wilusz, J. E., JnBaptiste, C. K., Lu, L. Y., Kuhn, C., Joshua-Tor, L., & Shapr, P. A. (2012). A triple helix stabilized the 3' ends of long noncoding RNAs that lack poly(A) tails. *Genes & Development*. 26, 2392-2407.

Yoshida, H., Matsui, T., Yamamoto, A., Okada, T., & Mori, K. (2001). XBP1 mRNA is induced by ATF6 and spliced by IRE1 in response to ER stress to produce a highly active transcription factor. *Cell*. 107, 881-891.

Yoshida, H., Okada, T., Haze, K., Yanagi, H., Yura, T., Negishi, M., & Mori, K. (2000). ATF6 activated by proteolysis binds in the presence of NF-Y (CFB) directly to the *cis*-acting element responsible for the mammalian unfolded protein response. *Molecular and Cellular Biology*. *20*(18), 6755-6767.

Zuker, M. (2003). Mfold web server for nucleic acid folding and hybridization prediction. *Nucleic Acids Research*. *31*(13), 3406-3415.

Chapter Two

Divergent Nucleotide Dependency of *S. cerevisiae* and *S. pombe* Ire1-KR

Introduction.

The accumulation of unfolded proteins in the endoplasmic reticulum (ER) activates the transmembrane protein Ire1. Direct binding of unfolded proteins to the Ire1 lumenal domain triggers its oligomerization which in turn stimulates trans-autophosphorylation of the cytosolic kinase domain, which together activate Ire1's cytosolic RNase domain (Gardner and Walter, 2011; Karagöz et al., 2017; Credle et al., 2005; Aragón et al., 2009; Korennykh et al., 2009). Binding of ligands to the kinase domain of *S. cerevisiae* Ire1 has been demonstrated to allosterically enhance the enzyme's RNase activity *in vitro* (Korennykh et al., 2011). ATP binds strongly to the kinase nucleotide-binding pocket and is used as a substrate for the kinase activity of Ire1, but binding of ATP does not fully trigger the RNase-activating conformational change. ADP binding does stimulate RNase activity *in vitro* by several orders of magnitude. It is compelling to speculate that Ire1 may sense the ADP/ATP ratio due to the higher activity of ADP bound to Ire1 compared to ATP, thus integrating the energy status of the cell into UPR signaling. Alternatively, an unidentified small molecule metabolite could serve biological roles in modulating Ire1 activity via binding the nucleotide pocket *in vivo*. Previous studies resolved two distinct steps in cofactor-Ire1 interactions: cofactor binding, and the conformational response of the protein (Korennykh et al., 2011). Activating cofactors bound to the nucleotide pocket stabilize the αC-helix in the active "in" position. This active conformation is tightly coupled to the beta-phosphate docking of bound nucleotide. Suboptimal beta phosphate docking, as in the case of a triphosphate, does not preclude the ligand from binding, but will not activate the *S. cerevisiae* enzyme. Whether the *S. pombe* Ire1 enzyme utilizes similar cofactor-mediated conformational activation has yet to be explored.

Results and Discussion.

***S. pombe* Ire1-KR can be activated by ATP analogs**

ADP has been shown previously to be a potent activator of *S. cerevisiae* Ire1 RNase activity (Korennykh et al., 2011). To test whether ADP activates *S. pombe* Ire1 in a similar way, we compared the RNase activity of *S. cerevisiae* Ire1-KR and *S. pombe* Ire1-KR *in vitro* following the site-specific cleavage of the same P^{32}-labeled RNA hairpin substrate derived from the *XBP1* 3' splice site (HP21) (Figure 2.1A). This substrate was chosen because it contains the CNG|CNGN motif in a 7-mer loop (where "|" indicates the Ire1 cleavage site) that is required by *S. cerevisaie* Ire1 and the UG|C motif that is required by *S. pombe* Ire1 (Gonzalez et al., 1999; Li et al., 2018). At saturating concentrations, ADP activated Ire1 from both species, though *S. pombe* Ire1 had a higher basal activity in the apo state on the HP21 substrate (Figure 2.1B). We next compared the activation of *S. pombe* and *S. cerevisiae* Ire1-KR by other cofactors to test if the *S. pombe* enzyme was similarly specific for the diphosphate nucleotide. We found that at saturating concentrations, the nucleotide ADP and synthetic cofactor APY29 (Korennykh et al., 2009) were the most potent activators of *S. cerevisiae* Ire1-KR, stimulating RNase activity 15-20 fold (Figure 2.1C). ADP and APY29 both strongly activated *S. pombe* Ire1-KR but only by ~10 fold (Figure 2.1D). The ADP analog ADPβS did not activate *S. cerevisiae* or *S. pombe* Ire1-KR. The sulfur substitution in this nucleotide introduces a "soft" atom, which has a larger covalent radius than that of oxygen. Sulfur does not form strong hydrogen bonds or coordinate strongly with hard cations such as magnesium (Forconi et al., 2008). When we supplied the soft cation manganese to the assay buffer, we observed restoration of RNase activity to the level of ADP•Mg^{2+} for enzymes from both organisms (Figure 2.1E). In the crystal structure of cytosolic *S. cerevisiae* Ire1 bound to ADP (PDB ID 2rio) (Lee et al., 2007), all three oxygens on the beta

phosphate form interactions essential for Ire1 activation. The beta phosphate coordinates with Mg^{2+} through one oxygen, forms a hydrogen bond with a conserved lysine K702 through the second oxygen, and forms a hydrogen bond to the backbone of a loop with the third. Because the analog ADPβS did not activate the *S. pombe* enzyme without addition of Mn^{2+}, the *S. pombe* Ire1 nucleotide binding pocket must also require all three interactions with the beta phosphate to stabilize the active conformation.

The non-hydrolysable and slow-hydrolyzing ATP analogs, AMPPNP and ATPγS respectively, did not stimulate the activity of the *S. cerevisiae* enzyme, but did activate the *S. pombe* enzyme to similar levels as ADP addition. The highly specific hydrogen bonding and metal coordination network in the nucleotide binding pocket cannot form with larger triphosphate nucleotides bound in the budding yeast enzyme. The specific residues identified to interact with the ADP beta phosphate and coordinate Mg^{2+} are conserved in *S. pombe* Ire1*,* but upstream of where the loop backbone contacts the nucleotide, there is a glutamate to proline mutation in the middle of the beta1 strand. Proline is a unique amino acid in that its side chain is covalently bonded to the backbone nitrogen. This forces a sharp turn in the backbone and also prevents backbone hydrogen bonds due to the lack of the amide proton (MacArthur et al., 1991; Joseph et al., 2013). Prolines are therefore mostly observed in loops, turns, and at the beginning of helices or strands. The glutamate to proline substitution may disrupt the beta-sheet and expand the nucleotide-binding pocket to accommodate the larger ATP analogs in the *S. pombe* enzyme and allow the interaction between the gamma phosphate at the protein backbone to form. To test this hypothesis, we created a *S. cerevisiae* Ire1-KR mutant in which we mutated the glutamate at position 677 to a proline to see if it would allow the *S. cerevisiae* enzyme to be activated by larger nucleotides similarly to the *S. pombe* enzyme. We found that the ATP analogs activated

the the *S. cerevisiae* Ire1-KR E677P mutant RNase activity by 3-4 fold compared to the WT *S. cerevisiae* Ire1-KR, though cleavage rate in the apo or ADP-bound state was unaffected (Figure 2.1F). This indicates that the point mutation allowed the enzyme to be activated by larger nucleotides.

Conclusions.

We have shown that *S. pombe* Ire1-KR will use ADP and synthetic molecules as cofactors in the same manner as *S. cerevisiae* Ire1-KR, indicating a similar coordination network in the nucleotide binding pocket between the two enzymes. Strikingly, the *S. pombe* Ire1-KR did not distinguish between di- and tri-phosphate nucleotides in terms of fold activation. We were able to identify a mutation that could give *S. cerevisiae* Ire1-KR this property of *S. pombe* Ire1-KR through disruption of a beta strand. It is intriguing to speculate about the functional consequence of these differences *in vivo*. If *S. cerevisiae* Ire1 is in fact discriminating between ADP and ATP in order to monitor energy levels in the cytosol, it would appear that the *S. pombe* enzyme is inert to such differences. It is possible that the enzymes do not generally use nucleotides as cofactors *in vivo*, but instead bind an unidentified stress-induced small molecule, in which case each enzyme's nucleotide binding pocket may have evolved to be optimized for binding of its respective cofactor.

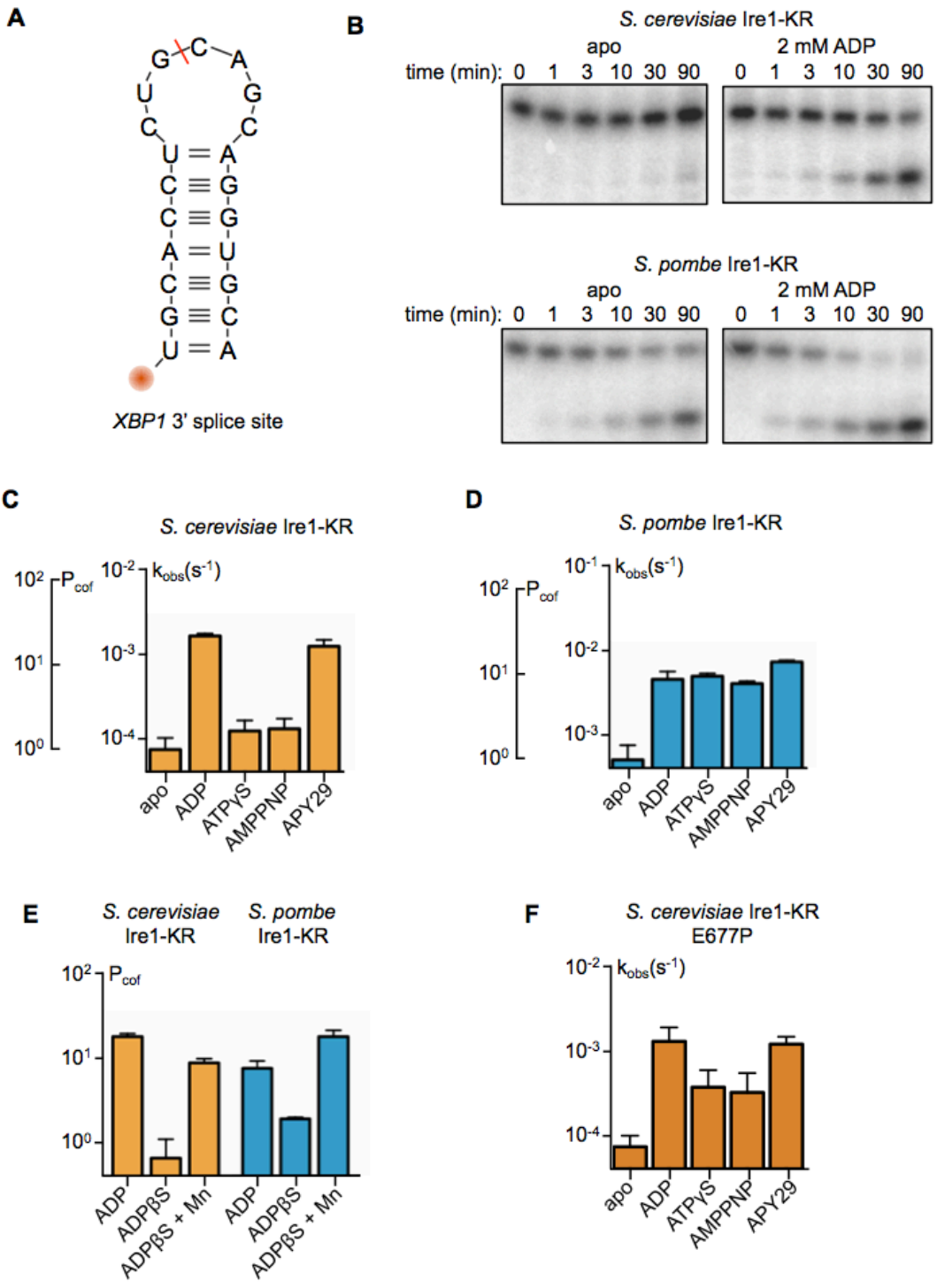

Figure 2.1. Cofactor-mediated activation of *S. pombe* and *S. cerevisiae* Ire1-KR
(**A**) Schematic representation of P^{32}-labeled RNA substrate used in this work. HP21 hairpin RNA is derived from *XBP1* 3' splice site. Red line marks site of specific cleavage by Ire1. (**B**) *In vitro* RNA cleavage assays. Radiolabeled HP21 was incubated with 11 μM *S. cerevisiae* or *S. pombe* Ire1-KR at 30°C with or without 2 mM ADP for the indicated amount of time. Reaction buffer contains (**C** and **D**) Cleavage rate (k_{obs})

calculated from cleavage assays as in (B) with one-phase decay fit. Substrate and *S. cerevisiae* Ire1-KR (C) or *S. pombe* Ire1-KR (D) were incubated with 2 mM of indicated nucleotide or analog. Potency of cofactor (P^{cof}) is defined as fold change in cleavage rate over apo state. (**E**) Cleavage rate as calculated in (C) and (D) with 2mM of indicated nucleotide or analog. All reactions contain 2 mM Mg^{2+}. Mn^{2+} was supplemented in the indicated reactions. (**F**) Cleavage rate as calculated in (C) of mutant *S. cerevisiae* Ire1-KR with glutamate at position 677 mutated to proline.

Materials and Methods.

Plasmid constructs and recombinant protein expression and purification

The cytoplasmic portion of *S. cerevisiae* or *S. pombe* Ire1p containing its kinase and RNase domains, Ire1-KR, was expressed and purified from BL21-CodonPlus (DE3)-RIPL *Escherichia coli.* We used an expression vector which fuses a PreScission Protease cleavage site between the Ire1p-KR and glutathione *S*-transferase (GST) domains of the recombinant polypeptide and was regulated by a T7 promoter. The expression cassette was transformed into *E. coli* cells and the *S. cerevisiae* protein was expressed as described previously (Korennykh et al., 2009). For cells transformed with the *S. pombe* Ire1-KR expression vector, all colonies on the transformation plate were collected 16 hrs after transformation and mixed with 50 mL of LB medium. After 3 hr incubation at 37°C, the sample was diluted to 12 L of LB medium and further incubated at 37°C until optical density reached 1. The incubation temperature was reduced to 25°C and protein expression was induced by adding IPTG to a final concentration of 0.5 mM. After 4 hrs of growth at 25°C, the cells were pelleted by centrifugation.

Cells were resuspended in GST binding buffer (50 mM Tris-HCl pH 7.5, 500 mM NaCl, 2 mM $Mg(OAc)_2$, 2 mM DTT, 10% Glycerol) and homogenized using high-pressure homogenizer (EmulsiFlex). The cell lysate was applied to a GST-affinity column and eluted with GST elution buffer (50 mM Tris-HCl pH 7.5, 200 mM NaCl, 2 mM $Mg(OAc)_2$, 2 mM DTT, 10% Glycerol, 10 mM reduced glutathione). The column elution was treated with GST-tagged HRV 3C protease (PreScission Protease, GE Health) to cleave the GST tag. At the same time, the sample was dialyzed to remove glutathione in the elution buffer. After 12 hr dialysis, the sample was further purified through negative chromatography by passing through a GST-affinity column (to remove free GST, residual GST-fused Ire1-KR, and GST-tagged protease)

and a Q FF anion exchange column (to remove contaminating nucleic acids). The flow-through containing untagged Ire1-KR was further purified by applying it to a Superdex 200 16/60 gel filtration column (GE healthcare) and then concentrated to 20-40 μM in storage buffer (50 mM Tris-HCl pH 7.5, 500 mM NaCl, 2 mM $Mg(OAc)_2$, 2 mM TCEP, 10% Glycerol) and flash frozen in liquid nitrogen. The final purity, as well as purity at intermediate steps, was assessed by SDS-PAGE using Coomassie blue staining.

***In vitro* RNA Cleavage Assay**

HP21 RNA oligos were purchased from Dharmacon, Inc. (UGCACCUCUGCAGCAGG UGCA). RNA oligos were gel extracted, acetone precipitated, and resuspended in RNase-free water. The oligos were 5'-end radiolabeled with gamma-[^{32}P]-ATP (Perkin Elmer) using T4 polynuclotide kinase (NEB) and cleaned using illustra MicroSpin G-25 Columns (GE Life Sciences). To fold the RNA, we heated the RNA oligos to 90°C for 3 min and slowly cooled them down at a rate of 1°C per minute until the temperature reached 10°C.

In the Ire1 cleavage assays, the reaction samples contained 11 μM of Ire1-KR. The cleavage reaction was performed as described previously (Li et al., 2018) by incubating at 30°C in reaction buffer (50 mM Tris/HCl pH 7.5, 200 mM NaCl, 2 mM $Mg(OAc)_2$, 2 mM TCEP, 10% Glycerol). At each time point, an aliquot was transferred to 1.2x STOP buffer (10 M urea, 0.1% SDS, 1 mM EDTA, trace bromophenol blue). RNAs were separated using denaturing 15% urea-PAGE gels (run at 100V for 90min) and transferred to Amersham Hybond-N+ membranes (GE Life Sciences). Radioactive RNA membranes were imaged with a Phosphorimager (Typhoon FLA 9500, GE Health). The band intensities were quantified using ImageJ. The cleaved portion was calculated as the cleaved band intensity divided by the sum of the cleaved band and

uncleaved band intensities. The k_{obs} were obtained by fitting the data to first-order 'one-phase' decay equations using Prism.

References.

Aragón, T., van Anken, E., Pincus, D., Serafimova, I. M., Korennykh, A. V., Rubio, C. A., & Walter, P. (2009). Messenger RNA targeting to endoplasmic reticulum stress signaling sites. *Nature*. *457*(5), 736-741.

Credle, J. J., Finer-Moore, J. S., Pap, F. R., Stroud, R. M., & Walter, P. (2005). On the mechanism of sensing unfolded protein in the endoplasmic reticulum. *Proceedings of the National Academy of Sciences*. *102*(52), 18773-18784.

Forconi, M., Lee, J., Lee, J. K., Piccirilli, J. A., & Herschlag, D. (2008). Functional identifications of ligands for a catalytic metal ion in group I introns. *Biochemistry*. *47*(26). 6883-6894.

Gardner, B. M. & Walter, P. (2011). Unfolded proteins are Ire1-activating ligands that directly induce the unfolded protein response. *Science*. 333, 1891-1894.

Gonzalez, T. N., Sidrauski, C., Dörfler, S., & Walter, P. (1999). Mechanism of non-spliceosomal mRNA splicing in the unfolded protein response pathway. *The EMBO Journal*. *18*(11), 3119-3132.

Joseph, P. R. B., Poluri, K. M., Gangavarapu, P., Rajagopalan, L., Raghuwanshi, S., Richardson, R. M., Garofalo, R. P., & Rajarathnam, K. (2013). Proline substitution of dimer interface b-strand residues as a strategy for the design of functional monomeric proteins. *Biophysical Journal*. 105, 1491-1501.

Karagöz, G. E., Acosta-Alvear, D., Nguyen, N. T., Lee, C. P., Chu, F., & Walter P. (2017). An unfolded protein-induced conformational switch activates mammalian IRE1. *eLife*. e30700.

Korennykh, A. V., Egea, P. F., Korostelev, A. A., Finer-Moore, J., Zhang, C., Shokat, K. M., Stroud, R. M., & Walter, P. (2009). The unfolded protein response signals through high-order assembly of Ire1. *Nature*. 457, 687-693.

Korennykh, A. V., Egea, P. F., Korostelev, A. A., Finer-Moore, J., Stroud, R. M., Zhang, C., Shokat, K. M., & Walter, P. (2011). Cofactor-mediated conformational control in the bifuncational kinase/RNase Ire1. *BMC Biology*. *9*(48).

Lee, K. P. K., Dey, M., Neculai, D., Cao, C., Dever, T. E., & Sicheri, F. (2007). Structure of the dual enzyme Ire1 reveals the basis for catalysis and regulation in nonconventional RNA splicing. *Cell*. 132, 89-100.

Li, W., Okreglak, V., Peschek, J., Kimmig, P., Zubradt, M., Weissman, J. S., & Walter, P. (2018). Engineering ER-stress dependent non-conventional mRNA splicing. *eLife*. e35388

MacArthur, M. W. & Thornton, J. M. (1991). Influence of proline residues on protein conformation. *Journal of Molecular Biology*. 218, 397-412.

Chapter Three

Divergent RNase activities of *S. cerevisiae* and *S. pombe* Ire1-KR

Introduction.

In higher eukaryotes, Ire1 has two functional outputs during the Unfolded Protein Response: (1) the conserved non-conventional cytosolic splicing of *XBP1* mRNA, which drives a large transcriptional program to increase the ER's protein-folding capacity (Yoshida et al., 2001; Calfon et al., 2002) and (2) the cleavage of a set of mRNAs encoding ER-targeted proteins that are then degraded, which reduces the ER folding burden in a process termed Regulated Ire1-Dependent Decay (RIDD) (Hollien and Weissman, 2006; Hollien et al., 2009). How these two outputs may be independently regulated in higher eukaryotes largely remains unknown. Although these two modalities coexist in metazoan cells, they are evolutionarily separated in the two yeast species *S. cerevisiae* and *S. pombe*. Ire1 in *S. cerevisiae* exclusively cleaves the mRNA encoding the Xbp1 homolog Hac1 to initiate a transcriptional program (Cox et al., 1993; Mori et al., 1993; Sidrauski et al., 1996), while in *S. pombe* there is no UPR transcription program. Rather, *S. pombe* Ire1 engages exclusively in RIDD (Kimmig and Diaz et al., 2012). The separation of these functional outputs is determined by the cytosolic domains of these proteins, as experiments using Ire1 chimeras revealed that swapping only the lumenal domains allowed the enzymes to be activated up ER stress, but swapping the cytosolic domains did not (Li et al., 2018). The Ire1 kinase/RNase domain from each species recognizes distinct RNA sequence and structural features. *S. cerevisiae* Ire1 cleaves a single substrate at two sites, one of which has previously been characterized to have a CNG|(C or A)NGN motif ("|" indicates Ire1 cleavage site) in a 7-mer loop (Gonzalez et al., 1999). In contrast, *S. pombe* Ire1 has possibly hundreds of substrates that only have a UG|C consensus motif in loops of variable sizes (Guydosh and Kimmig et al., 2017; Kimmig and Diaz et al., 2012; Li et al., 2018). The protein features responsible for the contrasting substrate scopes between the enzymes are explored here.

Results and Discussion.

Residues in the Ire1 RNase domain determine its RNase promiscuity.

We aimed at determining the molecular features that confer the promiscuous RNase activity of *S. pombe* Ire1. Because a previous study showed that the different RNase specificities of mammalian Ire1 alpha and beta are determined by their RNase domains (Imagawa et al., 2008), we compared the RNase domains of *S. cerevisiae* and *S. pombe* Ire1. Ire1's RNase activity is regulated by Ire1-RNA interactions and Ire1's oligomeric state (Korennykh et al., 2009; Li et al., 2010; Korennykh et al., .2011). As demonstrated by the crystal structure of *S. cerevisiae* Ire1, Ire1-RNA interaction and Ire1's oligomeric state are both modulated by specific structural elements (Lee et al., 2007; Korennykh et al., 2009; Korennykh et al., 2011). First, the Ire1-RNA interaction is modulated by the helix-loop element (HLE), which is a positively charged loop in the RNase domain that engages Ire1 with its RNA substrates. Second, Ire1's oligomeric state is modulated by dimer and oligomer interfaces. By comparing the amino acids near the HLE, dimer interface, and oligomer interface, we found a total of 17 amino acids in these regions that are significantly different between the *S. cerevisiae* and *S. pombe* Ire1 RNase domains (Figure 3.1A and B). These 17 residues are candidate residues that may determine Ire1's RNase specificity.

To test the combinatorial effects of the 17 candidate residues, we generated a *S. cerevisiae* Ire1 kinase/RNase mutant, which we call *S. cerevisiae* Ire1-KR mut-17 that has all of the 17 *S. cerevisiae* residues replaced by their *S. pombe* counterparts. We purified the recombinant *S. cerevisiae* Ire1-KR mut-17 and tested its RNase activity with four hairpin RNA substrates that we previously characterized (Li et al., 2018). One of the substrates is derived from the endogenous *S. cerevisiae HAC1* mRNA 3' splice site (Figure 3.1C). The other three are

derived from *S. pombe* Ire1 cleavage sites on *BIP1*, *PLB1*, *SPAC4G9.15* mRNAs (Figures 3.1D-F). We chose these three *S. pombe* substrates because their RNA stem loops, on which the Ire1 cleavage sites are located, vary in the loop sizes. Their loop sizes are 9-mer, 7-mer and 3-mer for *BIP1*-, *PLB1*- and *SPAC4G9.15*-derived RNAs respectively. The ability to cleave hairpin RNAs with variable loop sizes is a characteristic feature of the promiscuous *S. pombe* Ire1. In agreement with our previous result, the wild type *S. cerevisiae* Ire1-KR cleaved the *S. cerevisiae HAC1* mRNA 3' splice site but none of the *S. pombe* hairpin RNA substrates. Remarkably, the *S. cerevisiae* Ire1-KR mut-17 efficiently and specifically cleaved all four hairpin RNAs. Therefore, converting the 17 *S. cerevisiae* Ire1 residues to their *S. pombe* counterparts expands the RNA substrate scope of the *S. cerevisiae* Ire1.

Ire1 RNase promiscuity correlates with its toxicity to bacterial cells

Next, we set out to screen through the 17 candidate residues to identify which residue(s) confers RNase promiscuity. We sought an assay to exam RNase promiscuity that was time efficient and optimal for our screening purpose. To achieve this, we took advantage of a serendipitous observation that we had during our protein purification process. When recombinant *S. cerevisiae* Ire1 kinase/RNase domain (Ire1-KR) was expressed in *E. coli* cells, the cells grew normally at a rate comparable to that of a control strain bearing an empty plasmid. In contrast, when recombinant *S. pombe* Ire1-KR was expressed in *E. coli* cells, the cells showed a severe growth phenotype within the time window being examined. Given that *S. pombe* Ire1's RNase activity is more promiscuous than that of the *S. cerevisiae* Ire1, we hypothesized that the this promiscuity caused the toxic effects. To test this hypothesis, we inhibited *S. pombe* Ire1's RNase activity by adding a potent and specific Ire1 RNase inhibitor, 4μ8C, to *E. coli* cultures growing with the *S. pombe* Ire1-KR expression vector. Remarkably, 4μ8C completely inhibited the toxic

effects (Figure 3.2A). Furthermore, we observed that the *S. cerevisiae* Ire1-KR mut-17, which also has a promiscuous RNase, is toxic to bacterial cells as well. The toxicity can be similarly alleviated by adding the Ire1 RNase inhibitor (Figure 3.2B). Together, these results verified our hypothesis that Ire1 RNase promiscuity causes toxicity in bacterial cells: promiscuous RNases, like those of the *S. pombe* Ire1-KR and *S. cerevisiae* Ire1-KR mut-17, are toxic to bacterial cells while inactive or stringent Ire1 RNases, like that of the *S. cerevisiae* Ire1-KR, are not toxic. Therefore, Ire1's RNase promiscuity can be examined through bacterial growth assay, which is an efficient assay that is suitable for screening several Ire1 mutants at once.

Residues at the Ire1 RNase dimer interface regulate Ire1's RNase substrate specificity

To test which of the 17 candidate residues from the *S. pombe* Ire1 RNase domain were responsible for the expanded substrate repertoire of *S. cerevisiae* Ire1-KR mut-17, we individually converted the 17 *S. pombe* residues back to their original *S. cerevisiae* residues. We reasoned that if an *S. pombe* residue was necessary for the RNase promiscuity, reversing it to the corresponding *S. cerevisiae* residue would make the RNase more stringent. To this end, we generated 17 reverse mutants in which one of the 17 candidate residues was reversed in each mutant. Using the bacterial growth assay, we found that 14 of the 17 reverse mutants remained toxic, suggesting that the 14 corresponding residues were not necessary for the RNase promiscuity (Figure 3.2C). In contrast, three reverse mutants had reduced toxicity, suggesting that the three corresponding residues were required for the promiscuous RNase activity of *S. cerevisiae* Ire1-KR mut-17. These three residues are K992, H1044 and Y1059 on *S. cerevisiae* Ire1 and D950, D1001 and R1016 on *S. pombe* Ire1. To show that the three residues are sufficient to confer RNase promiscuity, we generated an *S. cerevisiae* Ire1-KR mutant called *S. cerevisiae* Ire1-KR mut-3 in which just the three residues (K992, H1044 and Y1059) were

replaced by their *S. pombe* counterparts. The *S. cerevisiae* Ire1-KR mut-3 was toxic to bacterial cells, confirming that the three mutated residues are sufficient for toxicity. In addition, the purified mutant protein efficiently cleaved the *S. pombe* hairpin RNA substrates and the endogenous *S. cerevisiae* hairpin RNA substrate *in vitro* (Figure 3.2D-G). Thus, converting the three *S. cerevisiae* residues to their *S. pombe* counterparts was sufficient to relax the RNase specificity.

Based on the locations of the three residues, they can be further classified into two groups. K992 and Y1059 of *S. cerevisiae* Ire1 (or D950 and R1016 of *S. pombe* Ire1) are located at the Ire1 dimer interface. H1044 of *S. cerevisiae* Ire1 (or D1001 of *S. pombe* Ire1) is located near the helix-loop element. We generated two *S. cerevisiae* Ire1 mutants based on this grouping. In one mutant, which we call *S. cerevisiae* Ire1-KR mut-IF, we converted the two dimer-interface residues to their *S. pombe* counterparts K992D and Y1059R. In the other mutant, which we call *S. cerevisiae* Ire1-KR mut-HLE, the residue near the helix-loop element was converted to its *S. pombe* counterpart H1044D. We found that the recombinant *S. cerevisiae* Ire1-KR mut-IF cleaved the *S. cerevisiae* and three *S. pombe* hairpin RNA substrates (Figure 3.2D-G). The interface mutant's cleavage efficiencies were similar to those of the parent mutant *S. cerevisiae* Ire1-KR mut-3. On the other hand, the *S. cerevisiae* Ire1-KR mut-HLE only cleaved the cognate *S. cerevisiae* RNA substrate, but none of the *S. pombe* RNA substrates. Therefore, we identified two residues at the Ire1 dimer interface that confer RNase promiscuity.

Residue 1044 was a false positive in our screen. Reversing the mutation in the context of the other 16 mutants could have had unexpected consequences on the protein structure, such as protein unfolding or other structural changes that could compromise the activity of the enzyme and thus suppress the toxicity of the parent protein.

The Ire1 interface mutant recognizes a distinct substrate motif

To comprehensively characterize the RNA substrate recognition motif of the *S. cerevisiae* Ire1-KR mut-IF, we examined a series of *HAC1*- and *BIP1*-derived mutant hairpin RNA substrates, in which each loop residue was individually changed into the three other possible ribonucleotides. Using the *HAC1*-derived mutant substrates, we verified that WT *S. cerevisiae* Ire1-KR recognizes a sequence motif of CNG|CNGN or CNG|ANGN located on a 7-mer stem loop, in agreement with previous findings (Gonzalez et al., 1999) (Figure 3.3A). It is worth noting that mutations at positions -4 or -5 (with respect to the Ire1 cleavage site) that break base-pairing in the stem and hence enlarge the loop, abolish cleavage. In comparison, the *S. cerevisiae* Ire1-KR mut-IF recognized a sequence motif of CNG|NNGN and tolerated larger loop sizes (Figure 3.3B). It was an unexpected finding that all mutations at position +1 were well-tolerated by the mutant protein, but mutations at positions -3 and +3 that were further away from the cleavage site were not.

Using the *BIP1*-derived mutant substrates, we verified that WT *S. pombe* Ire1-KR recognizes a sequence motif of UG|C on a step loop of variable size (Kimmig and Diaz et al., 2012; Li et al., 2018) (Figure 3.3C). Mutations at positions -5 or +4 that would reduce the loop from 9 bases to 7 by base pairing U-4 and G+5 were well tolerated by this enzyme. In comparison, the *S. cerevisiae* Ire1-KR mut-IF recognized a sequence motif of G|C for the *BIP1*-derived mutant (Figure 3.3D). It was similarly tolerant of changes in loop size as WT *S. pombe* Ire1-KR, but did not have a preference for the residue at position -2. Such a short substrate recognition motif would be highly prevalent in the transcriptome, even when coupled with the requisite structural stem-loop.

We had anticipated that the *S. cerevisiae* Ire1-KR mut-IF would have a single sequence motif shared by all its substrates. We predicted that this motif to be based on the consensus motif of the four substrates tested: G|C(A). It was unexpected both that the interface mutant had such a large motif for the *HAC1*-derived RNA hairpin and that these sequence requirements differed from those of the *BIP1*-derived RNA hairpin. Mutating the C in the +1 position on the *BIP1*-derived substrate to the residue found on the *HAC1* 3' splice site (A) abolished cleavage by *S. cerevisiae* Ire1-KR mut-IF. The enzyme was similarly intolerant of mutations at positions -3 or +3 on the *HAC1*-derived substrate to the residues found at those positions in the *BIP1* cleavage site. In fact the only element both substrates shared was a required guanine at the -1 position. The relative importance of these positions may be sensitive to the sequence context present in either loop.

An explanation for the discrepancy in the sequence requirements for these two substrates is that the enzyme may have two distinct binding modalities such that substrate binding depends on either a C at position +1 in the cleavage site or the peripheral C and G at positions -3 and +3 respectively. The *HAC1* 3' splice site-derived hairpin RNA may require these peripheral bases to interact with the enzyme while the *BIP1* cleavage site-derived substrate does not because it has the less favorable G|A sequence at the cleavage site. Substituting the adenine at the +1 position for a cytosine actually improved cleavage of the *HAC1*-derived substrate by the *S. cerevisiae* Ire1-KR, indicating that the WT sequence is not an optimal cleavage substrate, even for the WT enzyme.

The oligomeric state of *S. cerevisiae* Ire1-KR is modulated in the interface mutant.

The crystal structure of *S. cerevisiae* Ire1 shows that one of the residues mutated in *Sc* Ire1-KR mut-IF, K992, forms a salt bridge with another residue, E988, on a second monomer

across the dimer interface in the WT protein (PDB ID 2rio) (Lee et al., 2007) (Figure 3.4D, left and middle panels). We expected that replacing the positively charged lysine residue at position 992 with a negatively charged aspartate in the *S. cerevisiae* Ire1-KR mut-IF would disrupt this interaction and reduce the proclivity of the enzyme to dimerize. A more loosely packed RNase dimer may account for the ability of the mutant enzyme to cleave RNA hairpins with variable sized loops. To test how the mutation affects the dimerization of the protein, we tested the equilibrium oligomeric state of both WT proteins and the interface mutant. We measured the equilibrium constant of each protein by sedimentation equilibrium analytical ultracentrifugation (SE-AUC). Three concentrations of each protein (2.5 uM, 5 uM, and 10 uM) were allowed to reach equilibrium at three speeds (7,000, 10,000, and 14,000 rpm) and all nine datasets for each protein were globally fit to an equilibrium model. We found the WT *S. cerevisiae* Ire1-KR had a monomer-dimer equilibrium constant of 57.3 μM, indicating the protein had a weak affinity for itself (Figure 3.4A). The WT *S. pombe* Ire1-KR demonstrated a much higher propensity to oligomerize into significantly larger structures than observed for the *S. cerevisiae* protein (Figure 3.4B). It fit a monomer-octamer equilibrium with a constant of 0.0318 μM. The interface mutant fit a monomer-dimer equilibrium with a constant of 0.981 μM (Figure 3.4C), a significantly stronger affinity than the WT *S. cerevisiae* protein, though larger oligomers, as were seen in the WT *S. pombe* sample, were not detected.

We were surprised to find that *S. pombe* Ire1-KR had a much higher tendency to oligomerize than the *S. cerevisiae* enzyme. The *S. cerevisiae* Ire1-KR mut-IF was somewhat of an intermediate between the two; it had a lower monomer-dimer equilibrium constant than the WT *S. cerevisiae* protein but higher order structures that were apparent in the *S. pombe* Ire1-KR sample were not detected. *In vivo*, *S. cerevisiae* Ire1 has been shown to form large foci during

stress (Li et al., 2010). Although the kinase/RNase domain did not form higher order oligomers in this study, the contribution of the Ire1 linker domain has been shown to increase the propensity to oligomerize by several orders of magnitude. The contribution of the *S. pombe* Ire1 linker to oligomerization has not be evaluated. Our data suggests that *S. cerevisiae* Ire1 depends on the linker to provide critical interactions to form higher order structures, while the *S. pombe* Ire1 kinase/RNase domains are sufficient for oligomerization *in vitro*.

The mutated residues in *S. cerevisiae* Ire1-KR mut-IF form a putative salt bridge across the RNase domain dimer interface.

To predict how the interface mutations are affecting the oligomeric state of *S. cerevisiae* Ire1-KR, we performed Molecular Dynamic simulations on the RNase domains of WT *S. cerevisiae* Ire1 and *S. cerevisiae* Ire1 mut-IF. As expected, the simulations showed that the intermolecular interaction between residues 992 and 988 wasn't present in the mutant. In its place, however, was a salt bridge between the two mutated residues 992 and 1059 (Figure 3.4D, right panels). We hypothesize that this new interaction is responsible for the formation of more stable dimers and for the expanded substrate scope of the mutant protein. Whether these two features are coincidental or the higher oligomerization leads to promiscuity is unknown.

The Ire1 constructs we have been interrogating in these studies only consist of the cytosolic kinase/RNase domains. In other studies of *S. cerevisiae* Ire1, portions of the linker domain were included (*S. cerevisiae* Ire1-KR32) (Korennykh et al., 2009; Korennykh et al., 2011) and the protein was found to be several fold more active on its cognate *HAC1*-derived substrate and to oligomerize at much lower concentrations. *S. cerevisiae* Ire1-KR32, however, was not observed to be toxic to bacteria cells or have a broader substrate scope. Thus, although driving oligomerization may increase activity, it is not sufficient to relax substrate stringency. In

addition to stabilizing dimers, the putative salt bridge formed in the mutant between residues 992 and 1059 may cause subtle changes to the RNA binding site that increase its affinity for RNA hairpins that were not previously substrates of the WT protein.

Conclusions.

Here we have shown that we can modulate the specificity of *S. cerevisiae* Ire1-KR by making mutations in the RNase domain dimer interface. The mutant protein can cleave *S. pombe* substrates of variable loop sizes *in vitro* and has a lower dimerization equilibrium constant than the WT *S. cerevisiae* protein. The effects of these mutations on the monomer-dimer equilibrium echo previous studies on the effects of quercetin binding to IRE1 (Wiseman et al., 2010). The naturally-occurring flavonol quercetin was shown to be a potent activator *S. cerevisiae* Ire1 *in vitro*. This increase in RNase activity corresponded with a greater population of dimers. A crystal structure of quercetin:ADP:IRE1 revealed that it bound at the RNase interface, interacting with E988 and K992, two residues that form a salt-bridge that is disrupted by the mutations identified in our study. Quercetin binding to the RNase interface has similar effects on Ire1 as the mutations we describe here, though whether quercetin modified the enzyme's substrate specificity was not reported. The Ire1 RNase dimer interface could be exploited by future drug design or targeted mutations to manipulate mammalian Ire1 substrate specificity.

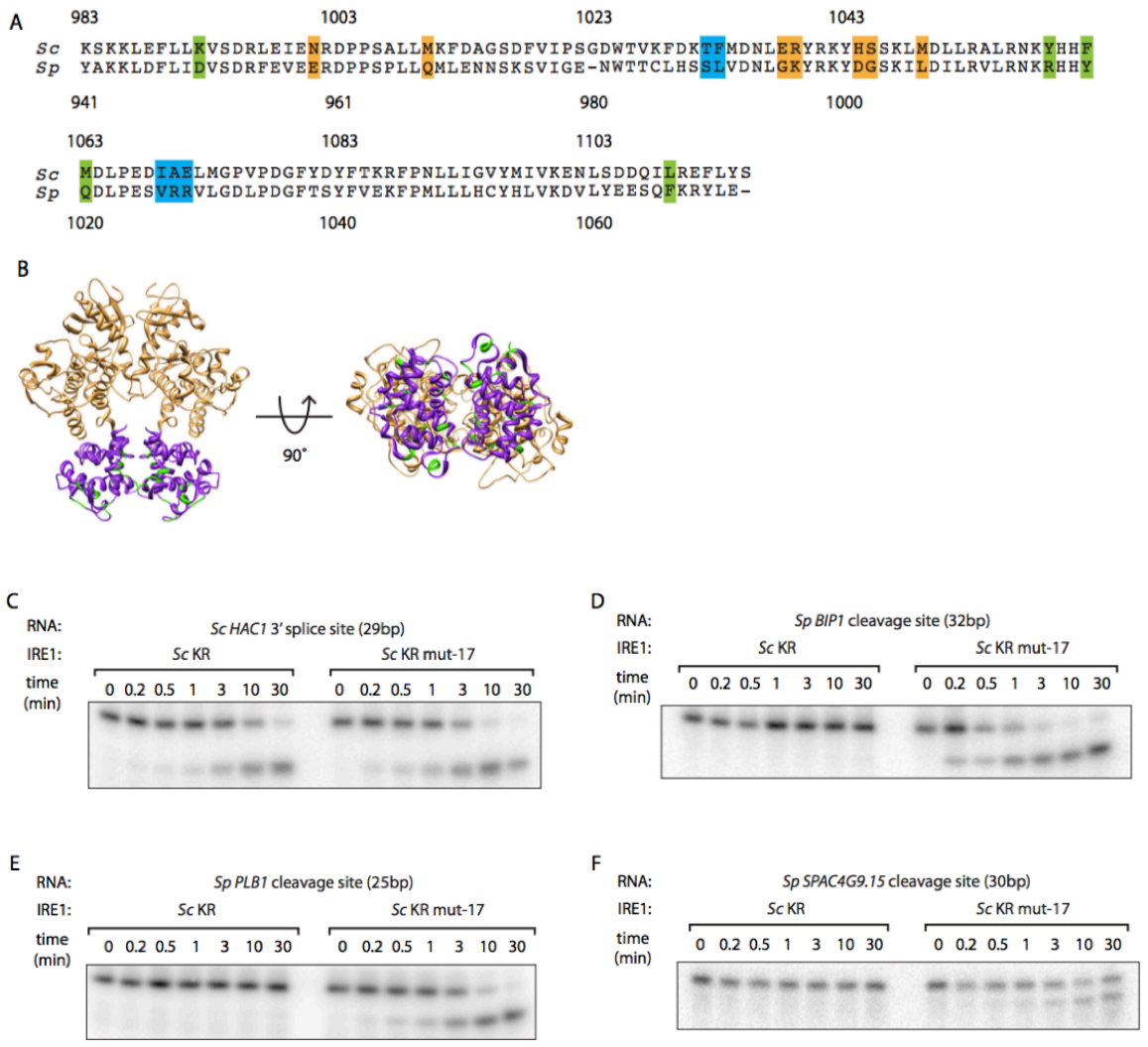

Figure 3.1. Mutations in the Ire1 RNase domain modulate its substrate specificity. (**A**) Alignment of *S. cerevisiae* and *S. pombe* Ire1 RNase domains. Candidate residues from the dimer interface are highlighted in green, from the oligomer interface are highlighted in blue, and from the helix loop element are highlighted in orange. (**B**) Structure of *S. cerevisiae* Ire1-KR (PDB ID 2rio). Kinase domain colored in gold, RNase domain in purple, and the 17 chosen residues in green. (**C-F**) *In vitro* RNase cleavage assays. 12.5 μM of WT *S. cerevisiae* Ire1-KR or mut-17 were incubated with 5'-radiolabeled hairpin RNA substrates derived from (**C**) the 3' splice site of *S. cerevisiae HAC1* mRNA, (**D**) the Ire1 cleavage site on *S. pombe BIP1* mRNA, (**E**) *PLB1* mRNA, and (**F**) *SPAC4G9.15* mRNA for indicated amount of time.

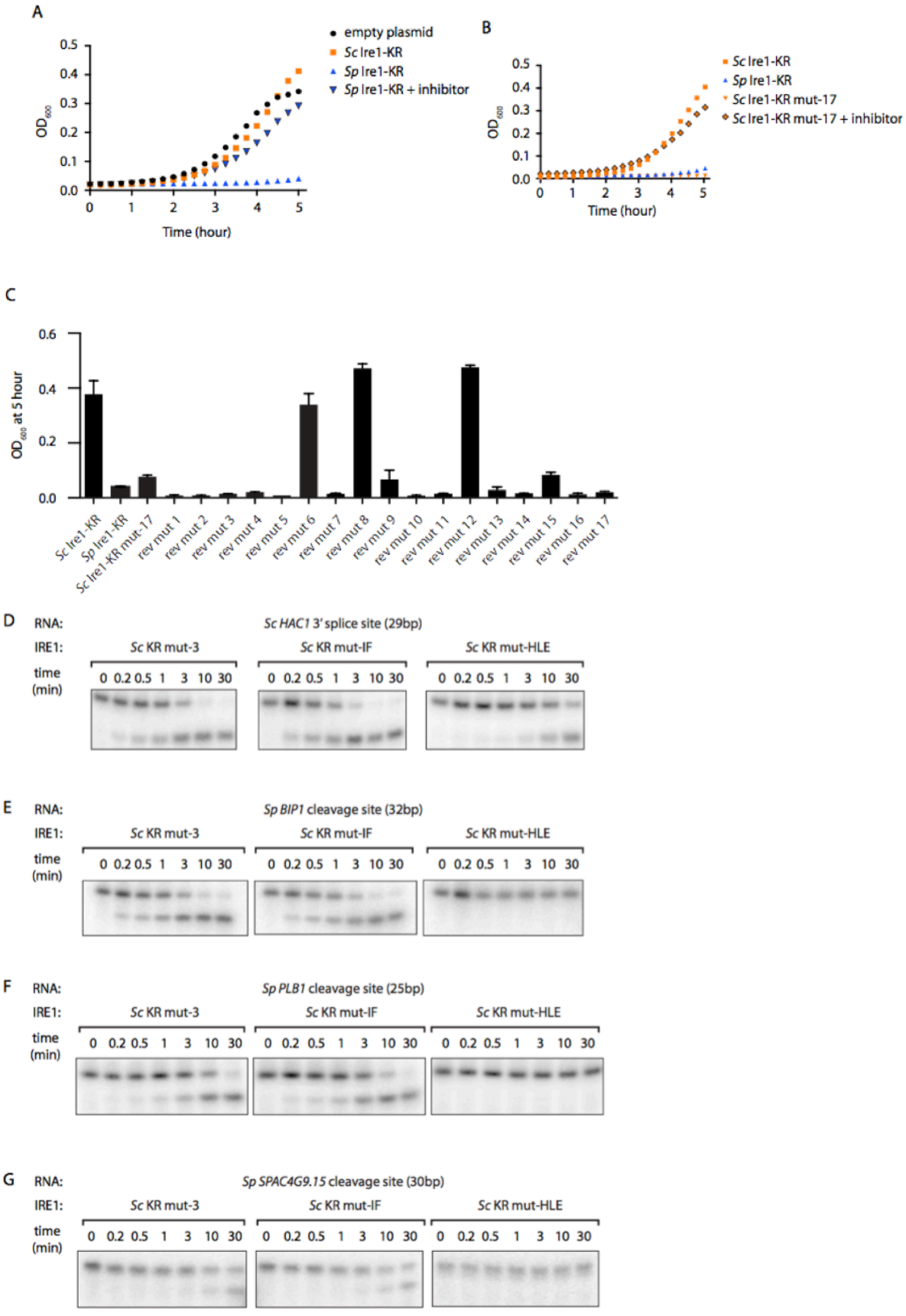
A
empty plasmid
Sc Ire1-KR
Sp Ire1-KR
Sp Ire1-KR + inhibitor
OD600
Time (hour)
B
Sc Ire1-KR
Sp Ire1-KR
Sc Ire1-KR mut-17
Sc Ire1-KR mut-17 + inhibitor
OD600
Time (hour)
C
OD600 at 5 hour
Sc Ire1-KR
Sp Ire1-KR
Sc Ire1-KR mut-17
rev mut 1
rev mut 2
rev mut 3
rev mut 4
rev mut 5
rev mut 6
rev mut 7
rev mut 8
rev mut 9
rev mut 10
rev mut 11
rev mut 12
rev mut 13
rev mut 14
rev mut 15
rev mut 16
rev mut 17
D
RNA:
Sc HAC1 3' splice site (29bp)
IRE1:
Sc KR mut-3
Sc KR mut-IF
Sc KR mut-HLE
time (min)
0 0.2 0.5 1 3 10 30
E
RNA:
Sp BIP1 cleavage site (32bp)
IRE1:
Sc KR mut-3
Sc KR mut-IF
Sc KR mut-HLE
time (min)
0 0.2 0.5 1 3 10 30
F
RNA:
Sp PLB1 cleavage site (25bp)
IRE1:
Sc KR mut-3
Sc KR mut-IF
Sc KR mut-HLE
time (min)
0 0.2 0.5 1 3 10 30
G
RNA:
Sp SPAC4G9.15 cleavage site (30bp)
IRE1:
Sc KR mut-3
Sc KR mut-IF
Sc KR mut-HLE
time (min)
0 0.2 0.5 1 3 10 30

Figure 3.2. Two residues at Ire1 dimer interface are responsible for Ire1's RNase substrate specificity.

(**A**) Bacterial growth assay showing that promiscuous Ire1 RNase activity is toxic to bacterial cells. Newly transformed *E. coli* cells were inoculated overnight, then diluted to OD 0.02 at time 0. The cell cultures were incubated at 37 degree for 5 hr and their OD were obtained every 20 min. *E. coli* cells carried an empty plasmid (black circles), a plasmid containing *S. cereivisiae* Ire1-KR (orange squares), or a plasmid containing *S. pombe* Ire1-KR (blue up triangles for growth assay without 4μ8c; blue down triangles for growth assay with 1 μM of 4μ8c added to both the overnight culture and the diluted culture). (**B**) Growth assay as in (A). *E coli* cells transformed with plasmid containing *S. cerevisiae* Ire1-KR (orange squares), *S. pombe* Ire1-KR (blue triangles), and *S. cerevisiae* Ire1-KR mut-17 (*S. cerevisiae* Ire1 KR mutant containing the 17 residues converted to the corresponding *S. pombe* residues) represented by orange diamonds and orange triangles for growth conditions with and without 4μ8c treatment respectively. (**C**) We reverted each mutation in *S. cerevisiae* Ire1-KR mut-17 to the WT residue one at a time and named these reverse mutants rev mut 1 to 17. Bacterial growth assays were performed with these reverse mutants under the same conditions as (A). The OD_{600} obtained at 5 hours was plotted. (**D-G**) *In vitro* RNase cleavage assays on 5'-radiolabeled hairpin RNA substrates. *S. cerevisiae* Ire1-KR mut-3, mut-IF, and mut-HLE were expressed, purified, and incubated with hairpin RNA substrates derived from (**D**) the 3' splice site of *S. cerevisiae HAC1* mRNA, the Ire1 cleavage site on *S. pombe* (**E**) *BIP1* mRNA, (**F**) *PLB1* mRNA and (**G**) *SPAC4G9.15* mRNA for indicated amount of time.

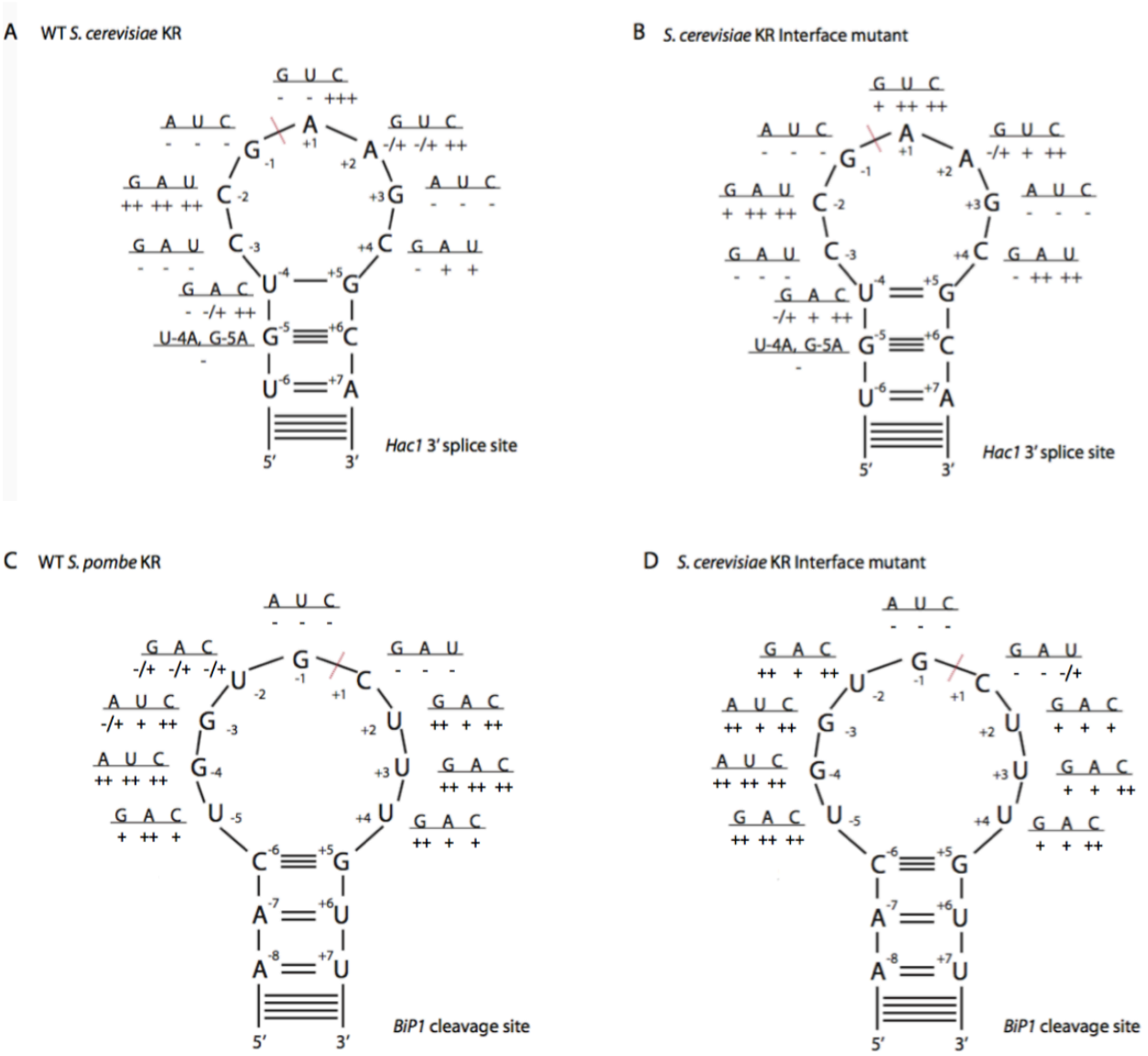

Figure 3.3. Mutational analysis of Ire1 cleavage substrates.
A series of stem-loop mutants derived from the *HAC1* 3' splice site (**A,B**) or the *BIP1* cleavage site (**C,D**) was transcribed and incubated with either WT *S. cerevisiae* Ire1-KR (**A**), WT *S. pombe* Ire1-KR (**C**) or the *S. cerevisiae* Ire1-KR interface mutant (**B,D**). The wild-type loop sequence is shown with each loop residue assigned a number relative to the Ire1 cleavage site indicated by a red dashed line. The sequence of the various point mutants is indicated next to each loop residue. Indicated below these sequences is the extent to which each mutant was cleaved by the indicated Ire1-KR protein as a fraction of the enzyme's cleavage of the wildtype stem-loop. Values are reported where (-) indicates no cleavage, (+/-) 0-10%, (+) 10-60%, (++) 60-120%, (+++) over 120%.

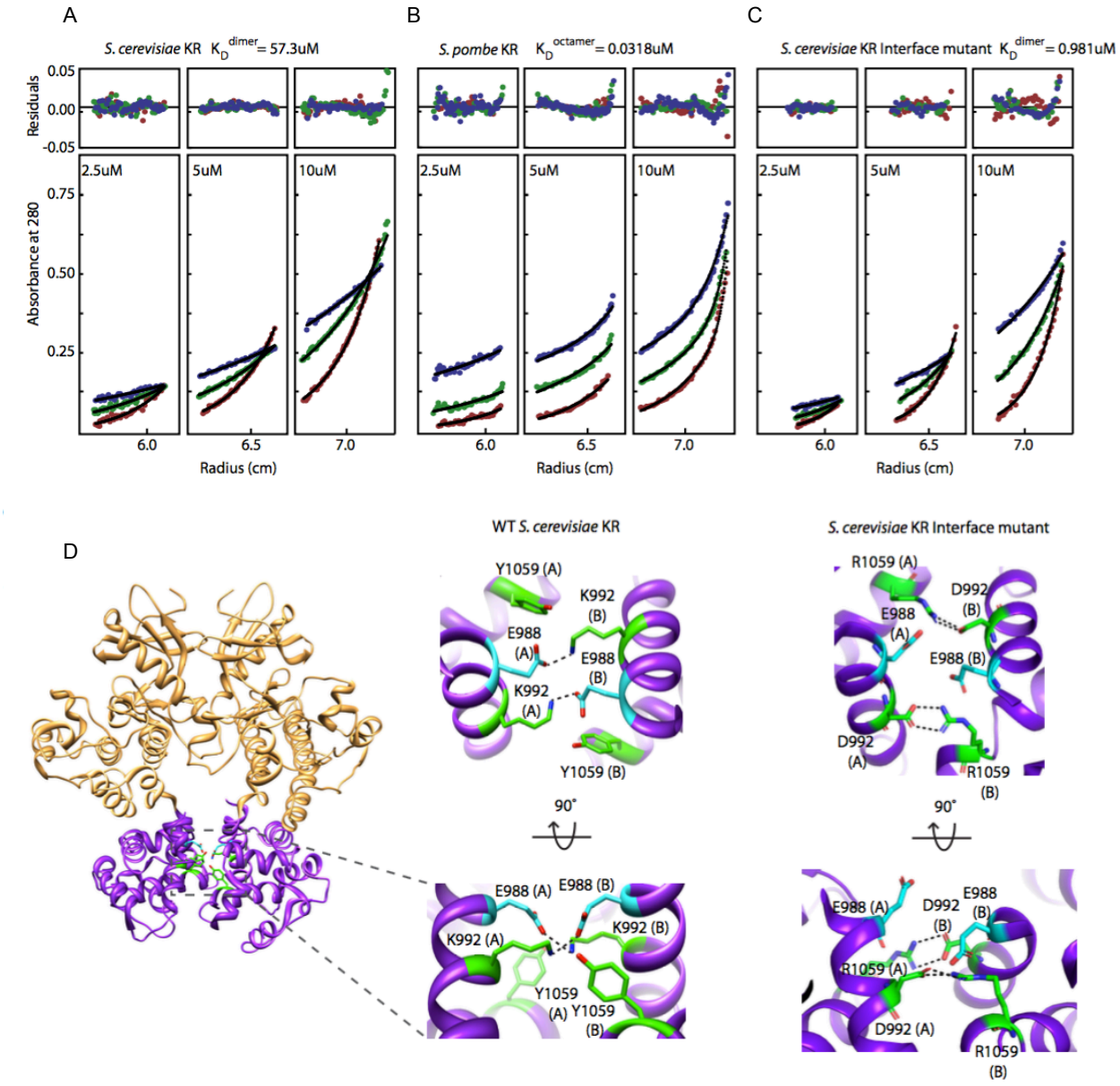

Figure 3.4. The *S. cerevisiae* Ire1-KR interface mutant is more prone to dimerize. (**A-C**) Sedimentation equilibrium analytical ultracentrifugation of WT *S. cerevisiae* Ire1-KR (**A**), WT *S. pombe* Ire1-KR (**B**), and *S. cerevisiae* Ire1-KR interface mutant (**C**). Absorbance data were collected at 280 at speeds of 7000 (blue dots), 10000 (green dots), and 14000 (red dots) rpm for proteins samples at 2.5 μM, 5 μM, and 10 μM (Lower panels). Raw data were trimmed using WinReEdit and globally fitted to an equilibrium model using WinNonlin. Residuals of curve fits (Upper panels). (**D**) Structure of *S. cerevisiae* Ire1-KR, colored as in figure 2b. Mutated residues from interface mutant (K992R and Y1059K) are colored in green. Residue E988 is colored in blue. Middle two panels show close up of WT *S. cerevisiae* RNase domain dimer interface from crystal structure (PDB=2rio). Right two panels show close up of RNase domain dimer interface from Molecular Dynamics Simulation *S. cerevisiae* Ire1 interface mutant.

Materials and Methods.

Plasmid constructs and recombinant protein expression and purification

The cytoplasmic portion of *S. cerevisiae* or *S. pombe* Ire1p containing its kinase and RNase domains, Ire1-KR, was expressed and purified from BL21-CodonPlus (DE3)-RIPL *Escherichia coli.* We used an expression vector which fuses a PreScission Protease cleavage site between the Ire1p-KR and glutathione *S*-transferase (GST) domains of the recombinant polypeptide and was regulated by a T7 promoter. The expression cassette was transformed into *E. coli* cells and the *S. cerevisiae* protein was expressed as described previously (Korennykh et al., 2009). For cells transformed with the *S. pombe* Ire1-KR expression vector or *S. cerevisiae* Ire1-KR mutants, all colonies on the transformation plate were collected 16 hrs after transformation and mixed with 50 mL of LB medium. After 3 hr incubation at 37°C, the sample was diluted to 12 L of LB medium and further incubated at 37°C until optical density reached 1. The incubation temperature was reduced to 25°C and protein expression was induced by adding IPTG to a final concentration of 0.5 mM. After 4 hrs of growth at 25°C, the cells were pelleted by centrifugation.

Cells were resuspended in GST binding buffer (50 mM Tris-HCl pH 7.5, 500 mM NaCl, 2 mM $Mg(OAc)_2$, 2 mM DTT, 10% Glycerol) and homogenized using high-pressure homogenizer (EmulsiFlex). The cell lysate was applied to a GST-affinity column and eluted with GST elution buffer (50 mM Tris-HCl pH 7.5, 200 mM NaCl, 2 mM $Mg(OAc)_2$, 2 mM DTT, 10% Glycerol, 10 mM reduced glutathione). The column elution was treated with GST-tagged HRV 3C protease (PreScission Protease, GE Health) to cleave the GST tag. At the same time, the sample was dialyzed to remove glutathione in the elution buffer. After 12 hr dialysis, the sample was further purified through negative chromatography by passing through a GST-

affinity column (to remove free GST, residual GST-fused Ire1-KR, and GST-tagged protease) and a Q FF anion exchange column (to remove contaminating nucleic acids). The flow-through containing untagged Ire1-KR was further purified by applying it to a Superdex 200 16/60 gel filtration column (GE healthcare) and then concentrated to 20-40 μM in storage buffer (50 mM Tris-HCl pH 7.5, 500 mM NaCl, 2 mM $Mg(OAc)_2$, 2 mM TCEP, 10% Glycerol) and flash frozen in liquid nitrogen. The final purity, as well as purity at intermediate steps, was assessed by SDS-PAGE using Coomassie blue staining.

***In vitro* RNA Cleavage Assay**

Short RNA oligos derived from the Ire1 cleavage site on *S. pombe BIP1* mRNA, *SPAC4G9.15* mRNA, *PLB1* mRNA, and the *S. cerevisiae HAC1* mRNA 3' splice site were purchased from Dharmacon, Inc. The sequence of hairpin RNA substrates ordered were the following: *Sp BIP1* cleavage site: 5'CGCGAGAUAACUGGUGCUUUGUUAUCUCGCG, *Sp SPAC4G9.15* cleavage site: 5'CCACCACCGAGUAUGCUACUCGGUGGUGG, *Sp PLB1* cleavage site: 5'…UUUGUUGCAAAAC…. (25bp), and *Sc HAC1* 3' splice site: 5'GCGCGGACUGUCCGAAGCGCAGUCCGCGC. RNA oligos were gel extracted, acetone precipitated, and resuspended in RNase-free water. The oligos were 5'-end radiolabeled with gamma-[^{32}P]-ATP (Perkin Elmer) using T4 polynuclotide kinase (NEB) and cleaned using ssDNA/RNA Clean and Concentrator kit (Zymo Research D7010).

In vitro transcription of the mutant RNA hairpins derived from the *HAC1* 3' splice site and *BIP1* cleavage site were carried out as follows. Singe-stranded DNA oligonucleotides were used as templates to which the 18mer 5'TAATACGACTCACTATAG "T7 promoter oligonucleotide" was annealed to create a double-stranded T7 RNA polymerase promoter. The templates used contain the indicated single point mutations from Figure 3.3 on the following

parent oligonucleotides: hac1-27 (encoding wild-type *HAC1* 3' stem-loop RNA with T7 promoter): 5'GCGCGGACTGCGTTCGGACAGTCCGCCTATAGTGAGTCGTATTA, and bip1-32 (encoding wild-type *BIP1* stem-loop RNA with T7 promoter): 5'CGCGAGATAACAAAGCACCAGTTATCTCGCGCTATAGTGAGTCGTATTA

A solution containing 5 nM T7 promoter oligonucleotide and 0.75 nM template oligonucleotide was heated to 100°C for 3 min and immediately placed on ice. 20 μL transcription reactions containing 5 μL of the template solution, 1 mM each of ATP, CTP, GTP, and UTP, 1x reaction buffer, and 2 μL T7 RNA Polymerase mix (HiScribe T7 High Yield RNA Synthesis Kit, NEB) were incubated at 37°C for 3hrs. RNA oligos were gel extracted in 300 μL RNase-free water.

To fold the RNA, we heated the RNA oligos to 90°C for 3 min and slowly cooled them down at a rate of 1°C per minute until the temperature reached 10°C. In the Ire1 cleavage assays, the reaction samples contained 12.5 μM of Ire1-KR. The cleavage reaction was performed as described previously (Li et al., 2018) by incubating at 30°C in reaction buffer (50 mM Tris/HCl pH 7.5, 200 mM NaCl, 2 mM $Mg(OAc)_2$, 2 mM TCEP, 10% Glycerol). At each time point, an aliquot was transferred to 1.2x STOP buffer (10 M urea, 0.1% SDS, 1 mM EDTA, trace bromophenol blue). RNAs were separated using denaturing 15% urea-PAGE gels (run at 100V for 90min) and trasferred to Amersham Hybond-N+ membranes. Radioactive RNA membranes were imaged with a Phosphorimager (Typhoon FLA 9500, GE Health). Non-radioactive RNA gels used in the substrate mutation analysis were imaged with SYBR Gold on the Typhoon with excitation at 488 nm; the emission was collected using a band pass filter at 550 nm. The band intensities were quantified using ImageJ. The cleaved portion was calculated as the cleaved band intensity divided by the sum of the cleaved band and uncleaved band

intensities. The k_{obs} were obtained by fitting the data to first-order 'one-phase' decay equations using Prism.

Bacterial growth assays

Expression vectors containing the *S. cerevisiae* Ire1-KR, *S. pombe* Ire1-KR, or a mutant form of these proteins regulated by a T7 promoter were transformed into *E. coli* cells. *E. coli* cells were inoculated overnight (~20 hrs) and then diluted to an OD_{600} of 0.02. The cultures were incubated at 37°C and their OD_{600} was obtained every 20 min by the Tecan Spark Multimode Microplate Reader (Life Sciences) (60 cycle kinetic loop, continuous shaking, double orbital 2.5 mm, 108 rpm) for 5 hrs. For cultures containing the Ire1 RNase inhibitor 4u8c, 1 μM of 4u8c was added into both the overnight culture and the diluted culture.

Analytical Ultracentrifugation

Experiments were performed in a Beckman Coulter Optima XL-A analytical ultracentrifuge equipped with UV-visible absorbance detection system using a 4-hole An-60 Ti analytical rotor. Multi-speed sedimentation equilibrium experiments were carried out at 20°C and 7,000, 10,000, and 14,000 rpm until equilibrium was reached for 110 μL samples of concentrations of 10 μM, 5 μM, and 2.5 μM protein. Samples were dialyzed overnight into analysis buffer (50 mM Tris/HCl, pH 7.5, 200 mM NaCl, 2 mM $Mg(AOc)_2$, 2 mM TCEP) to remove glycerol. Analysis buffer without protein was used as reference. Measurements were made at 280 nm in the absorbance optics mode. Raw data were trimmed using WinReEdit and globally fitted to a self-association equilibrium model using WinNonlin using all concentrations and speeds for each protein sample.

References.

Calfon, M., Zeng, H., Urano, F., Till, J. H., Hubbard, S. R., Harding, H. P., Clark, S. G., & Ron, D. (2002). IRE1 couples endoplasmic reticulum load to secretory capacity by processing the *XBP-1* mRNA. *Nature*. 415, 92-96.

Cox, J. S., Shamu, C. E., & Walter, P. (1993). Transcriptional induction of genes encoding endoplasmic reticulum resident proteins requires a transmembrane protein kinase. *Cell.* 73, 1197-1206.

Gonzalez, T. N., Sidrauski, C., Dörfler, S., & Walter, P. (1999). Mechanism of non-spliceosomal mRNA splicing in the unfolded protein response pathway. *The EMBO Journal*. *18*(11), 3119-3132.

Guydosh, N. R., Kimmig, P., Walter, P., & Green, R. (2017). Regulated Ire1-dependent mRNA decay requires no-go mRNA degradation to maintain endoplasmic reticulum homeostasis in *S. pombe*. *eLife*. e29216.

Hollien, J. & Weissman, J. S. (2006). Decay of endoplasmic reticulum-localized mRNAs during the unfolded protein response. *Science*. 313, 104-107.

Hollien, J., Lin, J. H., Li, H., Stevens, N., Walter, P., & Weissman, J. S. (2009). Regulated Ire1-dependent decay of messenger RNAs in mammalian cells. *The Journal of Cell Biology*. *186*(3), 323-331.

Imagawa, Y., Hosoda, A., Sasaka, S., Tsuru, A., & Kohno, K. (2008). RNase domains determine the functional difference between IRE1a and IRE1b. *Federation of European Biochemical Societies*. 582, 656-660.

Kimmig, P., Diaz, M., Zheng, J., Williams, C. C., Lang, A., Aragón, T., Li, H., & Walter, P. (2012). The unfolded protein response in fission yeast modulates stability of select mRNAs to maintain protein homeostasis. *eLife*. e00048.

Korennykh, A. V., Egea, P. F., Korostelev, A. A., Finer-Moore, J., Zhang, C., Shokat, K. M., Stroud, R. M., & Walter, P. (2009). The unfolded protein response signals through high-order assembly of Ire1. *Nature*. 457, 687-693.

Korennykh, A. V., Egea, P. F., Korostelev, A. A., Finer-Moore, J., Stroud, R. M., Zhang, C., Shokat, K. M., & Walter, P. (2011). Cofactor-mediated conformational control in the bifuncational kinase/RNase Ire1. *BMC Biology*. *9*(48).

Lee, K. P. K., Dey, M., Neculai, D., Cao, C., Dever, T. E., & Sicheri, F. (2007). Structure of the dual enzyme Ire1 reveals the basis for catalysis and regulation in nonconventional RNA splicing. *Cell*. 132, 89-100.

Li, W., Okreglak, V., Peschek, J., Kimmig, P., Zubradt, M., Weissman, J. S., & Walter, P. (2018). Engineering ER-stress dependent non-conventional mRNA splicing. *eLife*. e35388.

Li, H., Korennykh, A. V., Behrman, S. L., & Walter P. (2010). Mammalian endoplasmic reticulum stress sensor IRE1 signals by dynamic clustering. *Proceedings of the National Academy of Sciences*. *107*(37), 16113-16118.

Mori, K., Ma, W., Gething, M., & Sambrook, J. (1993). A transmembrane protein with cdc2^{+}/CDC28-related kinase activity is required for signaling from the ER to the nucleus. *Cell*. 74, 743-756.

Sidrauski, C., Cox, J. S., & Walter, P. (1996). tRNA ligase is required for regulated mRNA splicing in the unfolded protein response. *Cell*. 87, 405-413.

Wiseman, R. L., Zhang, Y., Lee, K. P., Harding, H. P., Haynes, C. M., Price, J., Sicheri, F., & Ron, D. (2010) Flavonol activation defines an unanticipated ligand-binding site in the kinase-RNase domain of IRE1. *Molecular Cell*. *38*(2), 291-304.

Yoshida, H., Matsui, T., Yamamoto, A., Okada, T., & Mori, K. (2001). XBP1 mRNA is induced by ATF6 and spliced by IRE1 in response to ER stress to produce a highly active transcription factor. *Cell*. 107, 881-891.

Publishing Agreement

It is the policy of the University to encourage the distribution of all theses, dissertations, and manuscripts. Copies of all UCSF theses, dissertations, and manuscripts will be routed to the library via the Graduate Division. The library will make all theses, dissertations, and manuscripts accessible to the public and will preserve these to the best of their abilities, in perpetuity.

Please sign the following statement:

I hereby grant permission to the Graduate Division of the University of California, San Francisco to release copies of my thesis, dissertation, or manuscript to the Campus Library to provide access and preservation, in whole or in part, in perpetuity.

Kelly J. Crotty
Author Signature

09.08.2019
Date